

Impact of Predictor Variables on Estimates of Global Sea-Air CO₂ Fluxes Using an Extra Trees Machine Learning Approach

Rik Wanninkhof¹, Joaquin Triñanes², Denis Pierrot³, David Russel Munro⁴, Colm Sweeney⁵, and Amanda R Fay⁶

¹OCD/AOML/NOAA

²Universidad de Santiago de Compostela

³Atlantic Oceanographic and Meteorological Laboratory

⁴University of Colorado Boulder

⁵NOAA Global Monitoring Laboratory

⁶Lamont-Doherty Earth Observatory, Columbia University

November 8, 2023

Abstract

Monthly global sea-air CO₂ flux estimates from 1998-2020 are produced by extrapolation of surface water fugacity of CO₂ (fCO_{2w}) observations using an Extra-trees (ET) machine learning technique. This new product (AOML-ET) is one of the eleven observation-based submissions to the second REgional Carbon Cycle Assessment and Processes (RECCAP2) effort. The target variable fCO_{2w} is derived using the predictor variables including date, location, sea surface temperature, mixed layer depth, and chlorophyll-a. A monthly resolved sea-air CO₂ flux product on a 1° by 1° grid is created from this fCO_{2w} product using a bulk flux formulation. Average global sea-air CO₂ fluxes from 1998-2020 are -1.7 Pg C yr⁻¹ with a trend of 0.9 Pg C decade⁻¹. The sensitivity to omitting mixed layer depth or chlorophyll-a as predictors is small but changing the target variable from fCO_{2w} to air-water fCO₂ difference has a large effect, yielding an average flux of -3.6 Pg C yr⁻¹ and a trend of 0.5 Pg C decade⁻¹. Substituting a spatially resolved marine air CO₂ mole fraction product for the commonly used zonally invariant marine boundary layer CO₂ product yield greater influx and less outgassing in the Eastern coastal regions of North America and Northern Asia but with no effect on the global fluxes. A comparison of AOML-ET for 2010 with an updated climatology following the methods of Takahashi et al. (2009), that extrapolates the surface CO₂ values without predictors, shows overall agreement in global patterns and magnitude.

Hosted file

978085_0_art_file_11540127_s3c185.docx available at <https://authorea.com/users/531155/articles/683918-impact-of-predictor-variables-on-estimates-of-global-sea-air-co2-fluxes-using-an-extra-trees-machine-learning-approach>

Hosted file

978085_0_supp_11540128_s3c186.docx available at <https://authorea.com/users/531155/articles/683918-impact-of-predictor-variables-on-estimates-of-global-sea-air-co2-fluxes-using-an-extra-trees-machine-learning-approach>

1
2
3
4 **Impact of Predictor Variables on Estimates of Global Sea-Air CO₂ Fluxes**
5 **Using an Extra Trees Machine Learning Approach**

6 **Rik Wanninkhof¹, Joaquin Triñanes^{1,2,3}, Denis Pierrot¹, David R. Munro^{4,5}, Colm**
7 **Sweeney⁴, and Amanda R. Fay⁶**

8 ¹Atlantic Oceanographic and Meteorological Laboratory, National Oceanic and Atmospheric
9 Administration, 4301 Rickenbacker Causeway, Miami, FL, USA.

10 ²Cooperative Institute for Marine and Atmospheric Studies, Rosenstiel School of Marine,
11 Atmospheric and Earth Science, University of Miami, 4600 Rickenbacker Causeway, Miami,
12 FL, USA.

13 ³Dept. of Electronics and Computer Science, Universidade de Santiago de Compostela, Santiago,
14 Spain

15 ⁴Global Monitoring Laboratory, National Oceanic and Atmospheric Administration, Boulder,
16 CO, USA

17 ⁵Cooperative Institute for Research in Environmental Sciences (CIRES), University of Colorado,
18 Boulder, CO, USA

19 ⁶Columbia University and Lamont Doherty Earth Observatory, Palisades NY, USA

20 Corresponding author: Rik Wanninkhof (rik.wanninkhof@noaa.gov)

21 †ORCID: 0000-0003-1973-3514.

22 **Key Points:**

- 23 • An Extra Trees machine learning approach, AOML_ET is described used to determine
24 global sea-air CO₂ fluxes.
25
26 • Global sea-air CO₂ fluxes from 1998-2020 are -1.7 Pg C yr⁻¹ with a trend of 0.9 Pg C
27 decade⁻¹.
28
29 • Comparison with other approaches and using different predictor variables show good
30 agreement in global fluxes but with large regional differences.
31

32 Abstract

33 Monthly global sea-air CO₂ flux estimates from 1998-2020 are produced by extrapolation of
34 surface water fugacity of CO₂ (fCO_{2w}) observations using an Extra-trees (ET) machine learning
35 technique. This new product (AOML_ET) is one of the eleven observation-based submissions to
36 the second REgional Carbon Cycle Assessment and Processes (RECCAP2) effort. The target
37 variable fCO_{2w} is derived using the predictor variables including date, location, sea surface
38 temperature, mixed layer depth, and chlorophyll-a. A monthly resolved sea-air CO₂ flux product
39 on a 1° by 1° grid is created from this fCO_{2w} product using a bulk flux formulation. Average
40 global sea-air CO₂ fluxes from 1998-2020 are -1.7 Pg C yr⁻¹ with a trend of 0.9 Pg C decade⁻¹.
41 The sensitivity to omitting mixed layer depth or chlorophyll-a as predictors is small but changing
42 the target variable from fCO_{2w} to air-water fCO₂ difference has a large effect, yielding an
43 average flux of -3.6 Pg C yr⁻¹ and a trend of 0.5 Pg C decade⁻¹. Substituting a spatially resolved
44 marine air CO₂ mole fraction product for the commonly used zonally invariant marine boundary
45 layer CO₂ product yield greater influx and less outgassing in the Eastern coastal regions of North
46 America and Northern Asia but with no effect on the global fluxes. A comparison of AOML_ET
47 for 2010 with an updated climatology following the methods of Takahashi et al. (2009), that
48 extrapolates the surface CO₂ values without predictors, shows overall agreement in global
49 patterns and magnitude.

50 Plain Language Summary

51 Surface water measurements of carbon dioxide (CO₂) are used to determine the global sea-air
52 flux of CO₂ across the interface for the time period from 1998-2020. The global flux direction is
53 into the ocean driven by atmospheric CO₂ increases caused by burning of fossil fuels and other
54 anthropogenic activities which affects the balance of the sea-air CO₂ gradient. While an
55 increasing number of surface ocean CO₂ observations are available, the data still requires
56 significant extrapolation/gap filling to characterize the entire global surface ocean on a monthly
57 basis. Here we describe a machine learning (ML) approach to create a monthly resolved surface
58 water CO₂ and flux product on a 1-degree grid using an extreme randomized trees or Extra Trees
59 approach, referred to as AOML_ET. AOML_ET is one of eleven observation-based submissions
60 to the second REgional Carbon Cycle Assessment and Processes (RECCAP2) effort. The global
61 scale results are compared to other available products and the sensitivity to different predictor
62 and target variables is described. Overall, there is strong agreement between approaches and
63 sensitivity to omitting certain target variables is small suggesting that on global scales the
64 approach is robust.

65 1 Introduction

66 Sea-air CO₂ fluxes are the main conduit for transfer and subsequent storage of anthropogenic
67 CO₂ in the ocean. The resulting increases in surface water CO₂ are the cause of surface ocean
68 acidification (Doney et al., 2020; Lida et al. 2021). Quantifying the fluxes is critical for the
69 global stocktake which reviews progress towards the Paris Agreement goals every five years
70 (Magnan et al., 2016), and to assess if the oceanic sink is changing on annual timescales,
71 particularly in light of the societal goal of reaching “net zero” by 2050 (IPCC, 2018).

72 Most regional and global sea-air CO₂ flux estimates on seasonal to annual scales rely on using
73 the bulk flux formulation where the flux density is the product of the gas transfer velocity, CO₂
74 solubility, and the fugacity difference of CO₂, or ΔfCO₂ between water (fCO_{2w}) and air (fCO_{2a})

75 (Eqn. 1). Here we use $f\text{CO}_2$ which accounts for the non-ideality of CO_2 gas rather than partial
76 pressure of CO_2 ($p\text{CO}_2$), except in the discussion of the updated Takahashi climatology.
77 Numerically $f\text{CO}_2 = 0.997 p\text{CO}_2$ at 25°C and the air-water $f\text{CO}_2$ difference, $\Delta f\text{CO}_2$ is essentially
78 the same as $\Delta p\text{CO}_2$, such that the results expressed in terms of $\Delta p\text{CO}_2$ can be directly compared.
79 The gas transfer velocity is commonly parameterized as a quadratic dependence with wind speed
80 (Wanninkhof, 2014). Surface water $f\text{CO}_2$ values are obtained using automated instrumentation
81 on a variety of ships and other platforms, such as moorings and autonomous surface vehicles.
82 The data are quality controlled and collated into communal data holdings, notably the Surface
83 Ocean CO_2 Atlas, SOCAT (Bakker et al., 2016) that is updated annually with an increase of over
84 1 million unique datapoints for each iteration ([https://www.socat.info/wp-](https://www.socat.info/wp-content/uploads/2022/06/2022_Poster_SOCATv2022_release.pdf)
85 [content/uploads/2022/06/2022_Poster_SOCATv2022_release.pdf](https://www.socat.info/wp-content/uploads/2022/06/2022_Poster_SOCATv2022_release.pdf)). The $f\text{CO}_{2w}$ data are binned,
86 gridded and interpolated/mapped to provide the foundation for global sea-air CO_2 flux fields,
87 often referred to as CO_2 flux maps. The interpolation in space and time is critical to obtain
88 uniform full coverage over the global ocean.

89
90 The initial interpolations of surface water $p\text{CO}_2$ data to estimate global sea-air CO_2 fluxes were
91 performed by Taro Takahashi and colleagues who determined global monthly $p\text{CO}_2$ maps and a
92 sea-air CO_2 flux climatology (Takahashi et al., 1997; 2009). The climatologies used much of the
93 available $p\text{CO}_2$ data at the time normalized to a particular year and presented per month on a 4°
94 by 5° grid. The empty cells were filled through interpolation to its neighbors aided by a modelled
95 surface ocean advection scheme (Bryan & Lewis, 1979). Here we present the Takahashi
96 climatology as submitted to RECCAP2 that is centered on reference year 2010, henceforth
97 referred to as Tak-2010. This climatology was recently updated by Fay et al. (2023, submitted)
98 using the same scheme and assumptions but with a larger dataset, the SOCATv2022 data
99 product. The climatology using a greater dataset and different approach for accounting for $f\text{CO}_{2w}$
100 increase through time by Fay et al. (2023) shows the same monthly spatial patterns and a global
101 flux of $-1.79 \pm 0.6 \text{ Pg C}$ in close agreement with Tak-2010 results presented here of -1.86 ± 0.52
102 Pg C . The Tak-2010 climatology, that is part of the RECCAP2 observation-based data holdings,
103 is chosen as a comparison in this study as it differs from other interpolation schemes in that the
104 $p\text{CO}_2$ data is interpolated/mapped without use of predictor variables. This is in contrast to the
105 various machine learning (ML) and linear regression approaches that rely heavily on the
106 predictor variables (Rödenbeck et al., 2015).

107
108 Much of the efforts in creating global sea-air CO_2 flux estimates have focused on approaches to
109 map $f\text{CO}_{2w}$ and subsequent comparisons and syntheses of the methods (Telszewski et al., 2009;
110 Landschützer et al., 2013; Zeng et al., 2014; Gregor et al., 2019; Stamen et al., 2020; Fay et al.,
111 2021). Significant improvement in these observation-based approaches have been made in the
112 last decade (Rödenbeck et al., 2015) notably through use of ML approaches for
113 interpolation/mapping of $f\text{CO}_{2w}$ along with an increase in available surface water measurements.
114 The products are commonly presented per month at 1° by 1° spatial resolution. These scales are
115 on the order of the autocorrelation scales of $f\text{CO}_{2w}$ (Li et al., 2005). The RECCAP2 analyses
116 include the output of eleven of such approaches with consistent protocols for nomenclature and
117 analysis. The recommended time range for the RECCAP2 surface water analysis spans years
118 from 1985-2018. The product described here covers the time period from October 1997 through
119 December 2020. The later start date is chosen because both the sparsity of $f\text{CO}_{2w}$ data, and the

120 inconsistent quality and coverage of predictor variables until the late 90s, most notably remotely
121 sensed chlorophyll estimates which became available from a common source at the end of 1997.

122
123 The extremely randomized trees or Extra Trees method (ET) used here (AOML_ET) is one of
124 several ML and regression approaches that use the same community assembled SOCAT
125 database. The SOCATv2020 product includes over 33 million unique $f\text{CO}_{2w}$ observations
126 collected from 1957 through 2021 (www.socat.info). However, for this analysis the gridded
127 SOCAT data product is used which consists of data collated into monthly 1° by 1° cells, reducing
128 the total to approximately 309 thousand data points. The eleven observation-based approaches
129 included in RECCAP2 regress the $f\text{CO}_{2w}$ from predictor variables, or use the predictor variables
130 in the training step of a ML technique. Interpolation is required due to sparse coverage of the
131 gridded SOCAT data product which has significant temporal and spatial gaps at the 1° by 1°
132 monthly resolution, particularly in the remote sections of the oceans and in winter seasons in the
133 mid- and high latitude oceans. Indeed, only about 2 % of the monthly 1° by 1° cells have $f\text{CO}_{2w}$
134 observations (Stamell et al., 2020). Predictor variables vary amongst approaches but surface
135 $f\text{CO}_{2w}$ values have been seen to closely correlate with sea surface temperature (SST) and mixed
136 layer depth (MLD). Sea surface salinity (SSS) and Chlorophyll-a (Chl-a) are often used as well.
137 These variables are known to directly influence $f\text{CO}_{2w}$ through biogeochemical and physical
138 interactions that control $f\text{CO}_{2w}$. Location (latitude, longitude) and time (yearday) are included in
139 the AOML_ET method to facilitate depiction of regional differences and trends. Atmospheric
140 mixing ratio of CO_2 ($X\text{CO}_{2a}$) has been used by other ML approaches as a time dependent
141 variable (e.g. Landschützer et al., 2016). Clustering or bagging approaches and delineation of
142 regions in specific biogeographical provinces or biomes (e.g. Fay & McKinley, 2014) have aided
143 the training and mapping in some ML and regression approaches but are not used in AOML_ET.

144
145 Different ML methods and other mapping products have been compared notably under the aegis
146 of the Surface Ocean CO_2 Mapping intercomparisons (SOCOM) effort (Rödenbeck et al., 2015)
147 and used in several assessments, including the global ocean carbon RECCAP2 effort (DeVries et
148 al., 2023). Detailed regional and global comparisons of different mapping products and ensemble
149 approaches have been undertaken (e.g. Fay et al., 2021; Gregor et al., 2019; Rödenbeck et al.,
150 2022; Chau et al., 2022). The analysis by Gregor et al. (2019) includes several different ML
151 approaches and suggests that overall skill of the methods at the global scale is similar and that
152 the skill for any given approach is mainly limited by $f\text{CO}_{2w}$ data availability in undersampled
153 regions and seasons. Gregor et al. (2019) also show broad similarity in magnitude and
154 interannual variability of $f\text{CO}_{2w}$ for the various ML approaches. In particular, the Northern
155 Hemisphere oceans show agreement between methods while areas with fewer $f\text{CO}_{2w}$
156 observations such as the mid- and high-latitude Southern Hemisphere oceans, and regions with
157 large interannual variability such as the Equatorial Pacific show greater differences between
158 approaches. Inconsistencies in modeled surface areas, wind speed products and the method of
159 calculation of fluxes contribute to differences. To account for these differences area
160 normalization and ensembles (or multi-product averages) are increasingly common in
161 intercomparison studies and improve consistency (Fay et al., 2021; Roobaert et al., 2018). A
162 summary of the annual global sea-air CO_2 fluxes for different ML approaches used in the Global
163 Carbon Budget (Friedlingstein et al., 2022) is provided in Figure 1 that show correspondence
164 over time between the observation-based methods at the global scale.

165

166 To date comparisons have often focused on the differences in the mapped $f\text{CO}_{2w}$ fields for the
167 different ML approaches, and the sea-air CO_2 fluxes derived from these fields using standard
168 indicators such as root mean square error (RMSE), bias, and the ability of the methods to
169 reproduce seasonal and interannual variability and trends at global and basin scales (Rödenbeck
170 et al., 2015; Gregor et al., 2019). Differences in flux products from other parameters used in the
171 bulk flux equation such as the gas transfer parameterization, as well as the sensitivity to different
172 predictor variables have been explored to lesser extent. The ET approach used here is
173 computationally efficient so that it lends itself to exploration of the impact of different variables.
174 Potential drawbacks of the ET method include that it can be more prone to bias in data sparse
175 regions compared to other ML methods. More specifically, with the ET approach observations in
176 regions with few data are viewed as outliers such that adjacent data further removed in time and
177 space receive greater weight (Gregor et al., 2019). It also shows a greater sensitivity to
178 overfitting than other commonly used ML approaches (Stamell et al., 2020; Gregor et al., 2019).

179
180 The paper is structured as follows: in the methods section we lay out the approach to determine
181 the sea-air CO_2 flux using the bulk flux formulation. The mapping of monthly $f\text{CO}_{2w}$ fields is
182 described using the analysis called AOML_EXTRAT_1998-2020, or AOML_ET for short. This
183 serves in part as documentation for the product submitted to RECCAP2. Of note is that the
184 AOML_ET RECCAP2 submission covers the time period 1998-2018 and this analysis is
185 extended by two years using the same procedures but with an updated SOCAT gridded dataset
186 (SOCATv2021). Different adaptations and predictor /target variables are described. The discussion
187 focusses on the seasonal and regional patterns observed in the AOML_ET product using an
188 analyses spanning a 22-year time series. A comparison with an updated climatology based on the
189 methods of Takahashi et al. (2009), Tak-2010, that was also submitted to RECCAP2 (DeVries et
190 al., 2023) is included. This climatological product is centered on 2010 and uses SOCAT data
191 from 1985-2018. The sensitivity of predictors to develop the $f\text{CO}_{2w}$ fields in AOML_ET
192 approach is discussed. Two different estimates of the mole fraction of CO_2 in air ($X\text{CO}_{2a}$) are
193 applied to determine the sensitivity of sea-air CO_2 fluxes to $X\text{CO}_{2a}$. The zonal-mean MBL
194 reference surface (MBL-RS) (Dlugokencky et al., 2021) that is used in many previous global
195 CO_2 flux estimates, including RECCAP2, is compared with the $X\text{CO}_{2a}$ derived from an
196 atmospheric CO_2 model, Carbon Tracker (Jacobson et al., 2020). The impact of two different gas
197 transfer-wind speed formulations is provided to illustrate the impact of the kinetic forcing of
198 fluxes which are not always considered when comparing the agreements of different sea-air CO_2
199 flux products. Some large scale diagnostics for sea-air fugacity difference and fluxes are also
200 presented. Fluxes presented are net CO_2 fluxes.

201 **2 Methodology**

202 *2.1 Determination of fluxes*

203
204 The $f\text{CO}_{2w}$ measurements are the foundation for determining the sea-air CO_2 fluxes but flux
205 estimates require other inputs such as the rate of CO_2 transfer across the sea-air interface and
206 CO_2 air concentrations as well. The sea-air CO_2 fluxes on regional to global scales are
207 determined using a bulk flux formulation where the flux density (F_{sa}) is defined as the product of
208 a thermodynamic term, the gradient across the interface ($\Delta f\text{CO}_2$), and a kinetic term, the gas
209 transfer velocity (k). The interpolation and gap filling methods focus on creating $f\text{CO}_{2w}$ fields,

210 and use canonical estimates for $f\text{CO}_{2a}$ and gas transfer parameterizations. The following
 211 expression for the bulk flux equation is applicable:

$$212 \quad F_{sa} = \overline{k K_0 (f\text{CO}_{2w} - f\text{CO}_{2a})} = \overline{k K_0 \Delta f\text{CO}_2} \quad (1)$$

214 where K_0 is the solubility of CO_2 in seawater. The $\Delta f\text{CO}_2$ is the difference between the fugacity
 215 that would be in equilibrium with water at 1 to 6 m below the interface, $f\text{CO}_{2w}$ and air, $f\text{CO}_{2a}$.
 216 The $f\text{CO}_{2a}$ is derived from a latitudinal averaged time series of mole fraction $X\text{CO}_{2a}$ of the
 217 marine boundary layer, MBL-RS (Dlugokencky et al., 2021). The overbar depicts the integrated
 218 quantity.
 219

220
 221 When calculating flux densities, the monthly $\Delta f\text{CO}_2$ fields at 1° by 1° grid are multiplied by the
 222 product of gas transfer velocity and solubility, thereby changing Eqn. (1) to:

$$223 \quad F_{sa} = \overline{k K_0 \Delta f\text{CO}_2} \quad (2)$$

224
 225 The Taylor expansion from the average of the product to averages of the individual terms has
 226 cross-correlation terms of k' and $\Delta f\text{CO}_2'$ but they are not included as they have a small influence
 227 on the overall results for determination of monthly global fluxes on scales of 1° (Wanninkhof et
 228 al., 2011).
 229

230
 231 The k is commonly parameterized as the square of wind speed (Wanninkhof et al., 2009):

$$232 \quad k = 0.251 \langle u^2 \rangle (Sc/660)^{-1/2} \quad \text{or} \quad k_{660} = 0.251 \langle u^2 \rangle \quad (3)$$

233
 234 where $\langle u^2 \rangle$ is the 2nd moment of the wind at 10-m height calculated from 6-hourly winds at $\frac{1}{4}^\circ$
 235 resolution (Hersbach et al., 2020); Sc is the Schmidt number, and 660 is the nominal Schmidt
 236 number of CO_2 at 20°C . The coefficient 0.251 is determined from scaling the gas transfer-wind
 237 speed relationship to the global average the 2nd moment of the wind and the inventory of bomb
 238 ^{14}C in the ocean (Sweeney et al., 2007).
 239

240
 241 The F_{sa} ($\text{mol m}^{-2} \text{y}^{-1}$) are aggregated into regional or global fluxes, with the flux expressed in Tg
 242 C (10^{12} g) or Pg C (10^{15} g = Gigaton). In the terrestrial and atmospheric communities bulk fluxes
 243 are often expressed as Tg or Pg of CO_2 where 1 Tg CO_2 equals 0.27 Tg C. For RECCAP2 the
 244 recommendation is that the sea-air flux be positive if the net flux is into the ocean, while in the
 245 oceanography community, and in this manuscript, the flux into the ocean (uptake) is presented as
 246 a negative value. The differences in conventions are summarized in Table A1.
 247

248 For the AOML_ET method monthly maps, or fields, of $f\text{CO}_{2w}$ are created after a training step
 249 and using predictor variables to determine the target $f\text{CO}_{2w}$ on monthly 1° by 1° grids. The ET
 250 ML algorithm is described in detail in Geurts et al. (2006). In short, it is based on a decision tree
 251 approach of learning much like the Random Forest approach. Its training uses a tree-based
 252 ensemble where nodes are split at random cut points using all observations to build the model.
 253

254 At a 1° by 1° monthly grid spacing there are 11.28 M possible grid nodes from October 1997
 255 through December 2020, but even for the best sampled months only a small fraction have $f\text{CO}_{2w}$

256 observations in the gridded in SOCATv2021 product. The maximum coverage is 4.3 % of all
257 cells for August 2011. For AOML_ET, 70 % of the data are placed into a training dataset, and 30
258 % are reserved for the testing dataset to determine bias and uncertainty expressed as a root mean
259 square error (RSME). Testing data include all the $f\text{CO}_{2w}$ observations from years 2000, 2005,
260 2010 and 2015. Omitting data from whole years is better than randomly withholding data points
261 for testing since this could lead to favoring test data in well sampled areas and seasons causing
262 uncertainty to not being appropriately represented.

263

264 *2.2 The Takahashi 2010 climatology*

265

266 To investigate seasonal and regional differences in sea-air CO_2 fluxes between approaches a
267 comparison is made between the AOML_ET for 2010 and the updated monthly Takahashi
268 climatology centered on 2010 (Tak-2010) created on a native resolution on a 4° by 5° grid and
269 subsequently sub-gridded to 1° resolution that is submitted to RECCAP2 (DeVries et al., 2023).
270 The creation of Tak-2010 follows the same procedures as the previous climatology centered on
271 year 2000 (Takahashi et al., 2009). It uses the same SOCAT dataset for $p\text{CO}_{2w}$ as the AOML_ET
272 analysis. In Tak-2010, the $p\text{CO}_{2w}$ values are adjusted to 2010 by assuming that $p\text{CO}_{2w}$ increases
273 at a similar rate as the atmospheric increase. Therefore, for $p\text{CO}_{2w}$ data between 1957 and 1979,
274 $1 \mu\text{atm y}^{-1}$ was added to each $p\text{CO}_{2w}$ observation; for 1980 through 2000, $1.5 \mu\text{atm y}^{-1}$ was
275 added; from 2001 through 2009, $2 \mu\text{atm y}^{-1}$ was added; and between 2011-2018, $2 \mu\text{atm y}^{-1}$ was
276 subtracted to normalize the $p\text{CO}_{2w}$ to the virtual year of 2010. The MBL-RS XCO_{2a} , P and SST
277 values for 2010 were used in the creation of flux maps. The interpolation in Takahashi et al.
278 (2009) is different from the gap filling in the ML and regression approaches in that it is done by
279 using a surface water advection scheme from a coarse resolution model (Bryan & Lewis, 1979)
280 without predictor variables. In contrast, all ML and regression methods used in RECCAP2 the
281 $f\text{CO}_{2w}$ rely on interpolated and gap filling using predictor variables.

282

283 *2.3 Sensitivity of sea-air CO_2 fluxes to different input variables*

284

285 Several adaptations of the AOML_ET default configuration are implemented to assess sensitivity
286 to procedures and predictor variables. The following changes are applied to the default
287 configuration of AOML_ET that uses location, time, SST, SSS, MLD, and Chl-a: The algorithm
288 was trained without Chl-a or without MLD; $\langle u^2 \rangle$ was added as a predictor; the algorithm was
289 trained against the target variable $\Delta f\text{CO}_2$ instead of $f\text{CO}_{2w}$. Using $\Delta f\text{CO}_2$ largely eliminates the
290 externally forced component, as $f\text{CO}_{2w}$ closely follows atmospheric CO_2 increases in the global
291 ocean (McKinley et al., 2020; Fay et al., 2023, submitted). Most of the adaptations did not yield
292 meaningful differences on global scales. A notable exception is substituting the target $f\text{CO}_{2w}$ for
293 $\Delta f\text{CO}_2$.

294

295 To determine the effect of data quality and quantity, a training dataset was created using only the
296 datasets flagged A and B in SOCATv2021 that have a stated accuracy of better than $2 \mu\text{atm}$,
297 compared to the default dataset that includes data flagged A-D where the C and D datasets are
298 estimated to be good to within $5 \mu\text{atm}$ (Wanninkhof et al., 2013). This decreases the total number
299 of grid cells with available data from 309,100 to 188,873 (Figure S1) and decreases coverage in
300 time, with no A, B data before 1990, and less data in high latitude and coastal regions (Figure
301 S2). As the uncertainty of the observations is not explicitly incorporated into the analyses, the

302 differences will primarily show up in lower data count and regional coverage, with a decrease in
 303 average number of cells with observations from 2.2 % to 1.5 % using only A and B data.

304

305 For investigating the impact of other variables needed to determine fluxes beyond those used to
 306 create $f\text{CO}_{2w}$ fields, the effect of using a different XCO_{2a} product is investigated as regional
 307 differences in XCO_{2a} can impact the fluxes (Wanninkhof et al., 2019). In the RECCAP2
 308 protocol, XCO_{2a} values from the MBL-RS are used with samples for XCO_{2a} taken weekly at 60
 309 sites around the globe forming the basis of this product
 310 (https://gml.noaa.gov/ccgg/about/global_means.html, Dlugokencky, 2021). These zonal averages
 311 are almost exclusively used in global CO_2 flux estimates.

312

313 In this zonally invariant MBL-RS product, the XCO_{2a} is expressed with time and latitude. To
 314 match the $f\text{CO}_{2w}$ resolution, the XCO_{2a} data is re-gridded on a monthly 1° by 1° grid and used to
 315 calculate $f\text{CO}_{2a}$ by:

316

$$317 \quad f\text{CO}_{2a} = G_f(T,S) (P - p\text{H}_2\text{O}) \text{XCO}_{2a} \quad (4)$$

318

319 where P is the barometric pressure at sealevel, $G_f(T,S)$ is the fugacity correction (≈ 0.996 to
 320 0.997 from 0 to 30°C) and $p\text{H}_2\text{O}$ is the saturation water vapor pressure at P and SST as
 321 summarized in Pierrot et al. (2009).

322

323 The default MBL-RS product is compared with XCO_{2a} over the ocean surface derived from
 324 CarbonTracker CT2019B (Jacobson et al., 2020). CT2019B provides a spatially and temporally-
 325 varying representation of XCO_{2a} throughout the atmosphere created by assimilating a wide
 326 variety of atmospheric CO_2 data in a 3-D atmospheric chemistry-transport model, TM5 (Krol et
 327 al., 2005). This CT-PBL product provides XCO_{2a} globally at 3-hourly intervals and at 3°
 328 longitude by 2° latitude spanning 2000-2020. The PBL height in TM5 is estimated from the
 329 ERA5 driving meteorology and a bulk Richardson number formulation (Jacobson and Munro,
 330 pers. com.) where the XCO_{2a} for each of the layers within the PBL is averaged. Then the 3°
 331 longitude by 2° latitude bins are regrided to a 1° by 1° and averaged monthly to determine the
 332 $f\text{CO}_{2a}$ (Eqn. 4) and the flux (Eqn. 1). This output is referred to as the CT-PBL product.

333

334 The effect of different wind speed products and parameterizations have been detailed in
 335 Roobaert et al. (2018), including discussion of the rationale for normalizing the wind products
 336 and gas transfer-wind speed dependencies. Two different parameterizations are compared here
 337 that differ in their assumptions of environmental forcing as detailed in Wanninkhof et al. (2009).
 338 A quadratic with zero intercept,

339

$$340 \quad k_{660} = 0.251 \langle u_{10}^2 \rangle \quad (5)$$

341

342 and a third-order polynomial dependency with wind with non-zero intercept, or hybrid
 343 parameterization,

344

$$345 \quad k_{660} = 3 + 0.1 \langle u_{10} \rangle + 0.083 \langle u_{10}^2 \rangle + 0.011 \langle u_{10}^3 \rangle \quad (6)$$

346

347 are compared. The coefficient for the 2nd moment of the wind has been adjusted in Eqn. 6 from
348 0.064 in the original equation of Wanninkhof et al. (2009) to 0.083 to account for the different
349 wind fields used between the original work and here. The parameterizations are shown versus
350 wind speed in Figure 2.

351 **3 Discussion**

352 The variability in sea-air CO₂ fluxes is largely driven by surface water fCO_{2w} but other drivers
353 can have an impact on the fluxes, particularly on regional scales. The salient features of the
354 fluxes based on the fCO_{2w} obtained with the AOML_ET method, as one of the eleven pCO₂
355 based approaches used in RECCAP2 (DeVries et al., 2023), are compared with Tak-2010. We
356 describe the sensitivity of the global sea-air CO₂ flux to different predictor variables and using
357 subsets of data. Comparisons of various ML approaches have been shown in other works (e.g.
358 Rödenbeck et al., 2015; Gregor et al., 2019; and Stammel et al., 2020) and will not be a focus
359 within.

360

361 *3.1 Global and regional trends in fluxes using the AOML_ET method*

362

363 A high level summary of results of the AOML_ET method are shown in Figure 3. The annual
364 global fluxes from 1998-2020 are shown in Figure 3a along with permutations of the method
365 described below. Figure 3b presents a Taylor diagram of observed and predicted values. For
366 AOML_ET a coefficient of correlation, r^2 of 0.83 was obtained, and a RMSE of 17 μatm in line
367 with other ML and regression estimates (Gregor et al., 2019). The standard deviation, indicating
368 the variability, is 34 μatm compared to 43 μatm for the observations.

369

370 Representative flux maps for the AOML_ET method for January and July 2010 provide a visual
371 depiction of spatial and seasonal differences in flux density (Figure 4) with well-described
372 features (e.g. Takahashi et al., 2009). The overall patterns and magnitude of AOML_ET fluxes
373 are in agreement with other data-based ML, regression approaches and climatologies used in
374 RECCAP2. There is outgassing in the tropical oceans and upwelling regions, and uptake in
375 subtropical and subarctic areas. Seasonal progressions are seen in the subtropics that change
376 from strong sinks in wintertime to a source in summer, primarily driven by changes in SST. A
377 strong source in the Bering Sea is prevalent in the wintertime, contrary to other Northern high
378 latitude regions that are wintertime sinks. This is attributed to deepening of the mixed layer in
379 winter entraining water with high CO₂. Overall, the winter season shows greater uptake than
380 summertime in the respective hemispheres. Globally, greatest uptake is in the December-
381 February timeframe.

382

383 The annual global fluxes from the AOML_ET approach falls within the range of other ML
384 methods albeit with a more negative global trend of $-0.9 \text{ Pg C dec}^{-1}$ than many of the approaches
385 (Figure 1, Table 1). This is, in part, attributed to the low fluxes at the beginning of the time
386 series, which combined with anthropogenic CO₂ emissions causing increasing fCO_{2a} leads a
387 larger sea-air CO₂ disequilibrium. That is, the ΔfCO_2 becomes more negative, and thereby
388 increases the CO₂ flux into the ocean and leads to a larger negative trend. Indeed, an inverse
389 relationship between the flux in 1998 versus trend is observed when comparing the different ML
390 methods (Figure 5) showing the negative feedback of low fluxes at the beginning of the record
391 for most approaches used in RECCAP2 leading to higher trends.

392
393 Differing trends in regional fluxes are apparent in the AOML_ET fluxes over the 1998-2020
394 time period. Significant areas show the expected negative trends (Figure 6a) with statistical
395 significance (Figure 6b). That is, the rising atmospheric CO₂ levels will cause greater uptake/less
396 outgassing, and thus a negative trend in fluxes. This negative trend is prevalent in the seasonally
397 stratified high latitude regions. Neutral and positive trends, that indicate less uptake or more
398 outgassing over time, are apparent in mid- and low-latitude regions and can be attributed to the
399 rise in SST and possible decrease in biological productivity (Landschützer et al., 2018). In broad
400 brush, the trends are in agreement with observation-based regional analyses of Fay and
401 McKinley (2013) that provide trends of fCO_{2w} instead of sea-air CO₂ fluxes shown here,
402 recognizing that positive trends in fCO_{2w} leads to smaller negative trends in flux. Their analysis
403 indicates that regions with a stronger trend in fCO_{2w} than expected from atmospheric increases
404 correspond to areas with increasing SST. They also show that regions with prevailing deep
405 (winter) mixed layers show smaller increases in fCO_{2w}, which are the regions of increasing
406 negative flux trends in our analysis.

407 408 *3.2 Comparison of AOML_ET with the Takahashi 2010 (Tak-2010)*

409
410 For this comparison the fluxes derived from AOML_ET in 2010 are compared to the climatology
411 of Takahashi centered on 2010. The fluxes determined in AOML_ET in 2010 and the Tak-2010
412 climatology are very similar in magnitude and pattern. For the global comparison of the
413 AOML_ET and Tak-2010, the surface areas are normalized. That is, the global fluxes in Tak-
414 2010 are scaled by 1.15 to account for the smaller ocean area covered. The global average sea-air
415 CO₂ flux and monthly variability expressed as the standard deviation of the monthly values in
416 2010 are -2.03 ± 0.46 and -1.86 ± 0.52 Pg C for the AOML_ET and Tak-2010, respectively.

417
418 The fluxes in both products show a seasonality with greatest uptake of about 0.2 Pg C mo⁻¹ from
419 November through March and smallest uptake of about 0.1 Pg C mo⁻¹ in August (Figures 7a,b).
420 Overall, the differences in global monthly uptake between products is small at less than 0.05 to
421 0.1 Pg C mo⁻¹, with largest differences in February-March (Figure 7c). The tropical regions
422 (14°S-14°N) are areas with persistent outgassing throughout the year in both products with Tak-
423 2010 showing greater outgassing during the boreal spring and summer compared to AOML_ET
424 (Figure 7). This is attributed, in part, to the fact that by nature Tak-2010 does not capture modes
425 of interannual variability such as caused by the El Niño Southern Oscillation (ENSO). The lower
426 outgassing within the 14°N to 14°S band in the boreal spring year of 2010 when El Niño
427 conditions persisted, as shown in AOML-ET in 2010, would not be reflected in Tak-2010. The
428 latter part of the year 2010 which experienced La Niña conditions shows very similar magnitudes
429 of fluxes in the tropics between products (Figures 7a,b). Similarities in products include that the
430 regions from 50°N to 14°N, and 50°S to 14°S are sinks, with wintertime for the respective
431 hemispheres showing greater uptake for both products. The exception is that 50°N to 14°N has
432 effluxes from July through September. The high latitudes (> 50°N/S) are areas with persistent
433 sinks with summertime showing the largest negative fluxes in line with increased biological
434 productivity drawing down the surface water fCO_{2w} (Takahashi et al., 2009). In the seasonal ice
435 zone (> 62 °S) wintertime uptake is negligible, largely because of ice cover.

436

437 Figure 7c provides a bar chart of the differences between AOML_ET in 2010 and Tak-2010 per
438 zonal region where small differences in monthly fluxes between products are attributed to
439 differences in the extrapolation/gap filling method applied to the $f\text{CO}_{2w}$ values as gas transfer
440 velocities and $f\text{CO}_{2a}$ are the same. Of note is that the differences are zonally compensating with
441 adjacent regions of both positive and negative differences in each month and bands partially
442 offsetting each other. Aside from differences in the tropical region described above, there are
443 also small differences between the AOML_ET and Tak-2010 products in the 14°N - 50°N and
444 14°S - 50°S regions. In the 14°N - 50°N zonal band the AOML_ET product shows less uptake for
445 much of the year except from July through September when the region outgasses for both
446 products but with greater outgassing in Tak-2010 (Figure 7b,c). The differences between 15°S
447 and 50°S largely counteract the differences to the north except from October through December
448 when AOML_ET shows less uptake compared to Tak-2010.

449
450 The subpolar divergence zone and marginal ice zones in the Southern Hemisphere represented
451 by the bands from 50°S - 62°S and $>62^{\circ}\text{S}$ are postulated to represent a CO_2 source based on
452 calculated values of $f\text{CO}_{2w}$ from pH sensors on profiling floats (Gray et al., 2018; Bushinsky et
453 al., 2019). Few data exist in this region within the SOCAT database, particularly in wintertime
454 such that the flux values reported for these regions will largely be dependent on gap filling. Both
455 products show uptake in the summer months (November-March) and less uptake in the winter.
456 The subpolar divergence zone in the Tak-2010 climatology shows weak outgassing while the
457 AOML_ET shows a weak sink. Physically, a source is expected in this area due to upwelling of
458 deep water with high CO_2 values, thus, the results here suggest that the training data for
459 AOML_ET is insufficient to train the algorithm for this region, and that the climatology
460 interpolation with an advection scheme provides a slightly better representation. Overall, the two
461 very different approaches of data utilization and gap filling show reasonable agreement
462 suggesting that different interpolation/gap filling approaches do not have a determining effect on
463 zonal fluxes even in data sparse regions.

464

465 *3.3 Sensitivity of $f\text{CO}_{2w}$ to predictor variables and change of target variable*

466

467 The different interpolation methods, and differences in the resulting $f\text{CO}_{2w}$ and flux maps have
468 been discussed by others (Fay et al., 2021; Gregor et al., 2019; Stamell et al., 2020 and
469 references therein) and we limit our discussion to the AOML_ET output only. Quantitatively
470 assessing the sensitivity of $f\text{CO}_{2w}$ to predictor variables in the ET method is challenging due to
471 inherent cross correlations between variables. Thus we use feature importance to assess the
472 influence of predictor variables to construct $f\text{CO}_{2w}$ fields (Figure 8). Location, expressed as the
473 sum of Latitude (LAT); and vector longitudes, sine (SLON) and cosine (CLON), with a score of
474 0.35, has the greatest importance, in part because no bagging or clustering is performed on the
475 $f\text{CO}_{2w}$ data, other than the initial binning in the creation of the monthly 1° by 1° SOCAT product.
476 This is followed by SST with a score of 0.22. This strong dependence of $f\text{CO}_{2w}$ with SST is
477 similar to most other gap filling techniques (Bennington et al., 2022), due to the strong physical
478 and chemical dependency of $f\text{CO}_{2w}$ with temperature with $\partial f\text{CO}_{2w} \partial T^{-1} = 0.042$ (Wanninkhof et
479 al., 2022). Time (Julian day, JDN) is the main driver of trends due to the increasing atmospheric
480 CO_2 levels over time. While several gap filling approaches, notably MLR interpolations, have
481 shown weak correlation with Chl-a, Chl-a is important in construction of the AOML_ET with a
482 score of 0.1. The other predictor variables, MLD, and SSS, each have similar scores of ≈ 0.1 .

483
 484 The impact of omitting predictor variables on global CO₂ fluxes is summarized in Figure 3a
 485 which shows AOML_ET output created without MLD and separately without Chl-a. These
 486 predictor values were selected for omission as their quality and resolution are of lower fidelity
 487 than the other predictors, particularly at the start of the record. MLD are model derived and Chl-a
 488 is a satellite ocean color product interpolated for regions and times with cloud cover. Overall,
 489 with these predictor variables omitted, no large impacts are seen in the global annual averages
 490 with all runs showing approximately the same magnitude, variability and trends, within their
 491 monthly variability of 0.3 Pg C y⁻¹ (Figure 3a). Omitting Chl-a increases the annual global uptake
 492 by about 0.2 Pg C y⁻¹ up to 2018 after which the global uptake decreases by 0.3 Pg C y⁻¹ between
 493 2018 and 2020 compared to the default AOML_ET configuration. Omitting MLD has a much
 494 smaller global effect with differences < 0.1 Pg C y⁻¹ for the record up to 2018 after which the
 495 uptake follows the same pattern as omitting Chl-a. Adding the second moment of the wind <u²>
 496 as a predictor variable does not show any differences with the default AOML_ET, except from
 497 2018 onward when uptake using <u²> is about 0.1 Pg C y⁻¹ greater than the default.

498
 499 In contrast, a large difference in the magnitude of global fluxes was observed when training with
 500 ΔfCO₂ as a target variable instead of fCO_{2w}. Resulting net sea-air CO₂ fluxes are -3 Pg C in 1998
 501 and -4 Pg C in 2020 or approximately 2 to 1.5 Pg C y⁻¹ greater uptake than the default
 502 AOML_ET version. (Figure 3a). The trend in the flux with time is less as well compared to the
 503 default configuration. The trend for the ΔfCO₂ target run from 1998-2020 is -0.55 Pg C y⁻¹
 504 decade⁻¹ compared to -0.9 Pg C y⁻¹ decade⁻¹ for the default AOML_ET product. The trend using
 505 ΔfCO₂ is more in line with other ML approaches that show an average trend of -0.7 Pg C y⁻¹
 506 decade⁻¹ since 1998 (Table 1). The cause for the poor agreement in magnitude of the global flux
 507 combined with the lower trend using ΔfCO₂ instead of fCO_{2w} is unclear. Changes ΔfCO₂ over
 508 time are expected to be relatively small with time as on decadal timescales the fCO_{2w} closely
 509 tracks fCO_{2a} due to the relatively rapid equilibration time of surface waters with the marine
 510 boundary layer of 3-6 months. This could explain the lower trend but as noted the large flux
 511 should lead to decreasing the ΔfCO₂ over time and cause a strong feedback that would not
 512 maintain such a flux.

513
 514 As shown in the Taylor diagram (Fig 3b) the different permutations do not appreciably impact
 515 the RMSE, variability (as expressed as a standard deviation of all data over the 23-year
 516 timespan) or correlation coefficient, r² of fCO_{2w} with all simulations showing a RMSE between
 517 18 and 22 μatm; a r² between 0.83 and 0.88 and a standard deviation between 33 and 37 μatm
 518 compared to the standard deviation of data on 42 μatm (Figure 3b). The run where ΔfCO₂ is used
 519 instead of fCO_{2w} as the target variable instead of fCO_{2w} shows the best statistics with a RSME of
 520 18 μatm, a standard deviation of 37 μatm, and r² of 0.88. However, as noted above the magnitude
 521 and trend of the fluxes determined in this configuration is very different from the default
 522 configuration with magnitudes not consistent with other available products (DeVries et al.,
 523 2023).

524 525 *3.4 Sensitivity to data quality and quantity*

526
 527 The product using the AOML_ET procedure with the gridded data comprised of datasets flagged
 528 A and B with accuracy better than 2 μatm shows small differences with the default product with

529 slightly smaller uptake ($\approx 0.2 \text{ Pg C y}^{-1}$) over the first part of the record and from 2013 onward
530 (Figure 3a). Using only higher quality data lead to less gridded data points and slightly degrades
531 statistics (Figure 3b) with an r^2 of 0.82 and RMSE of $22 \mu\text{atm}$. The default AOML_ET product
532 has a r^2 of 0.87 and a RSME of 20. The A,B product also shows less variability at $33 \mu\text{atm}$
533 compared to $35 \mu\text{atm}$ of the default AOML_ET product for the 1998-2020 time period. The
534 slightly reduced variability can, in part, be explained by the fact that the higher quality data is
535 generally from the open ocean that exhibits less variability than the coastal seas. As suggested in
536 Hauck et al. (2023), the SOCAT database contains more near-shore data in the latter part of the
537 record with lower $f\text{CO}_{2w}$ values and larger variability. This leads to a possible artifact in
538 estimating trends and variability using the full SOCAT dataset. A more thorough analysis is
539 required to separate the impacts of using a subset of higher quality data versus the resulting
540 reduced number of observations. In particular data denial approaches are a powerful means of
541 investigation.

542

543 *3.5 Sensitivity to $f\text{CO}_{2a}$*

544

545 Sea-air CO_2 fluxes are very sensitive to the magnitude of the $\Delta f\text{CO}_2$ ($=f\text{CO}_{2w}-f\text{CO}_{2a}$). A bias in
546 $\Delta f\text{CO}_2$ of $1 \mu\text{atm}$ globally will change the global annual sea-air CO_2 flux by $\approx 0.2 \text{ Pg C}$. The
547 $f\text{CO}_{2a}$ are often measured in conjunction with $f\text{CO}_{2w}$, but fluxes are commonly derived using an
548 independent XCO_{2a} that is zonally averaged, like the MBL-RS. However, the zonal homogeneity
549 in XCO_{2a} is not reflected in $f\text{CO}_{2a}$ (Eqn. 4) with systematic regional differences in barometric
550 pressure (P) and saturation water vapor pressure ($p\text{H}_2\text{O}$). These can cause zonal differences up to
551 $\approx 16 \mu\text{atm}$ in $f\text{CO}_{2a}$ even with constant XCO_{2a} (Figure 9). The P and $p\text{H}_2\text{O}$ will both affect the
552 $f\text{CO}_{2w}$ and $f\text{CO}_{2a}$ in a similar fashion such that errors in P and $p\text{H}_2\text{O}$ will not have a large impact
553 on $\Delta f\text{CO}_2$ as long as the same P and SST products are used to calculate both $f\text{CO}_{2w}$ and $f\text{CO}_{2a}$.
554 Variability in $f\text{CO}_{2w}$ in the open ocean is up to 10 times larger than $f\text{CO}_{2a}$. However, systematic
555 differences in $f\text{CO}_{2a}$ can be of importance due to the small global sea-air disequilibrium of ≈ -6
556 μatm (Figure 10) driving the fluxes.

557

558 During fall and winter months, air flowing off continents generally has higher CO_2 due to fossil
559 fuel burning and net ecosystem respiration on land. This leads to higher XCO_{2a} over many
560 coastal seas and larger influxes/lower effluxes, particularly along the heavily industrialized
561 eastern continental boundaries in the Northern Hemisphere due to the prevailing westerly winds
562 at those latitudes. During spring and summer, however, carbon uptake on land due to terrestrial
563 photosynthesis can lead to negative zonal anomalies in XCO_{2a} which causes decreased ocean
564 uptake, especially in coastal regions. Northcott et al. (2019) showed from extrapolating
565 nearshore observations that the higher PBL XCO_2 could enhance global ocean CO_2 uptake by 1
566 %.

567

568 The impact of higher XCO_{2a} in coastal regions can be discerned by using the spatially resolved
569 CT-PBL product compared to the zonally averaged MBL-RS product. Of note is that this effect
570 will be quantitatively similar for fluxes derived for all the different ML and interpolation
571 approaches. The difference in CT-PBL product versus the MBL-RS product on global scales is
572 small because the global averages of XCO_{2a} between the MBL-RS and CT-PBL products are
573 similar. The global monthly ocean sink differences using the CT-PBL compared to the MBL-RS
574 XCO_2 from 2000-2020 are $-0.02 \pm 0.05 \text{ Pg C}$ with the CT-PBL product showing slightly greater

575 fluxes into the ocean on average. No appreciable year-to-year differences are observed. The
 576 regional differences can be large with this change, particularly in the winter months. The largest
 577 differences are off the East Coasts of North America and Asia. Figure 11 shows the differences
 578 in the 30-35°N latitude band for 2010 between fluxes derived from the MBL-RS and CT-PBL as
 579 a representative example. The entire latitude band shows the characteristic seasonal pattern for
 580 the subtropics with a strong sink in winter and weak source in summer with an annual average
 581 for 2010 of $-0.61 \text{ mol m}^{-2} \text{ y}^{-1}$ for the MBL-RS product and $-0.66 \text{ mol m}^{-2} \text{ y}^{-1}$ for the CT-PBL
 582 product. The Mid Atlantic Bight (MAB) off the coast of the USA (30-35°N, 75-70°W) and
 583 Yellow Sea (30-35°N, 120-125°W) show wintertime enhancement of uptake by 6 and 21 %,
 584 respectively in agreement with a similar exercise performed by Palter et al. (2023, accepted
 585 GRL). The differences in spring and summer are smaller with the MAB showing a slightly
 586 decreased influx during May for the CT-PBL attributed to $\text{XCO}_{2\text{a}}$ drawdown on land due to the
 587 springtime increase in terrestrial biological productivity.

588

589 *3.6 Sensitivity to the gas transfer velocity*

590

591 Different gas transfer velocity formulations and wind speed products can impact the global flux
 592 estimates with past studies indicating that this is a primary source of uncertainty in global flux
 593 estimates (Woolf et al., 2019). The impact of time averaging and the effect of different wind
 594 fields has been investigated (Wanninkhof et al., 2002; Roobaert et al., 2018; and Gregor et al.,
 595 2019) but conical quadratic wind speed relationships to parameterize gas transfer are used in
 596 most flux estimates, including those in RECCAP2 (DeVries et al., 2023) and the GCB
 597 (Friedlingstein et al., 2022). A common procedure is to normalized the coefficient in the
 598 relationship (Eqn. 5) to a global average wind and gas transfer velocity value (Fay et al., 2021).
 599 Less emphasis has been placed on different functionalities of parameterizations (Wanninkhof et
 600 al., 2009). The different functionalities are of increasing importance with improved high
 601 resolution wind speeds and ΔfCO_2 mapped products such that the variability of ΔfCO_2 and $\langle u^2 \rangle$
 602 are better represented. Two gas exchange wind parameterizations are compared which are both
 603 in accord with the global ocean bomb ^{14}C inventories. The default parameterization is depicted in
 604 Eqn. 5, and the polynomial expression is shown in Eqn. 6 that is sometimes listed as a hybrid
 605 dependency. The rationale of the two parameterizations based on the controls of gas transfer at
 606 the interface is described in Wanninkhof et al. (2009).

607

608 The results show negligible global flux differences of $0.003 \pm 0.011 \text{ Pg C}$ between a quadratic
 609 dependency with wind, (Eq. 5) and hybrid expression (Eqn. 6). The uncertainty is captured in the
 610 standard deviation of annual differences from 1998-2020. While the results are the same on
 611 global scale, the different gas transfer parameterizations show significant differences in regional
 612 patterns of fluxes. Figure 12 shows maps of differences in fluxes between the quadratic and
 613 hybrid relationships for January and July 2010. The hybrid expression shows larger fluxes in
 614 select tropical and other low wind, doldrum, regions with winds persistently less than 5 m s^{-1} .
 615 These are areas with mostly effluxes of CO_2 . The effect of lower winds in the Northern
 616 Hemisphere tropical and subtropical regions during July is apparent compared to the windier
 617 times in the boreal winter (Figure 12b). Only few regions show larger fluxes at high winds (\approx
 618 13 m s^{-1}) with the hybrid expression. Notably, parts of the Bering Sea in January 2010 show
 619 higher fluxes with the hybrid parameterization and since the region has positive ΔfCO_2 , the
 620 hybrid parameterization leads to higher effluxes. Mid-latitude regions with prevailing winds

621 between 5 and 13 m s⁻¹ will have lower k_{660} with a hybrid parameterization and correspondingly
622 show lower fluxes.

623 **4 Conclusions**

624 The AOML_ET method described here is one of the observation-based fCO₂ approaches used in
625 RECCAP2 to interpolate fCO_{2w} observations into uniform fields, and determine global sea-air
626 CO₂ fluxes on monthly 1° by 1° resolution. The ET approach may suffer from spurious results in
627 under sampled regions compared to other ML mapping approaches. However its merits include
628 transparency and computational efficiency. The average flux of the AOML_ET method falls in
629 line with other approaches but with a greater long term trend from 1998-2000 and slightly less
630 interannual variability than other ML methods. The results for the year 2010 compare favorably
631 in terms of both the magnitude of the flux and seasonal and regional variability with the
632 Takahashi climatology centered on 2010. The analysis of using a different subset of the SOCAT
633 database based on quality criteria shows broad similarities but less variability with the higher
634 quality observation subset, likely because the high quality-only dataset is distributed more
635 heavily in the open ocean. Therefore, the impact of higher quality data cannot be clearly
636 discerned in this exercise as use of only higher quality data corresponds to lower data density
637 which also may lead to lower variability in general. The changes in RMSE and r² for the
638 different permutations of predictor and target values summarized in Figure 3b show no
639 appreciable differences in flux estimates on global scales, but differences show up in regional
640 patterns. The regional differences often are compensation leading to the good correspondence on
641 global scales. This agrees with other analyses (e.g. Gregor et al., 2019) who show that that the
642 different ML approaches yield similar global estimates. While agreement is encouraging, a
643 caveat is that the same gridded fCO_{2w} dataset is used such that the true uncertainty in fluxes is
644 likely underestimated. Similar predictors are used in all ML approaches and uncertainty and
645 biases in predictor values are often not incorporated into the uncertainty estimates. Largest
646 differences in ML approaches are apparent in the trends and are correlated with the magnitude of
647 fluxes at the beginning of the record, which in this analysis is 1998.

648 **Acknowledgments**

649 We acknowledge the Global Carbon Project, which is responsible for the Global Carbon Budget
650 and thank the ocean fCO₂-mapping groups for producing and making available their fCO₂-
651 product output which are used in Figure 1. The AOML_ET product was developed as
652 contribution the RECCAP2 effort. We appreciate the input of Andy Jacobson NOAA/GML,
653 CIRES for providing the CT-PBL boundary layer XCO₂ product and reviewing the section of
654 this manuscript utilizing the product. Observations from over 100 investigators worldwide are
655 collated in SOCAT that are the observational basis for this work. The many researchers and
656 funding agencies responsible for the collection of data and quality control are thanked for their
657 contributions to SOCAT. We thank Leticia Barbero (CIMAS/AOML) for internal review. The
658 NOAA office of Oceanic and Atmospheric Research is acknowledged for financial support, in
659 particular the Global Ocean Monitoring and Observations (fund reference 100007298)

660

661 **Open Research**

662 The AOML_ET results (1998-2018) and Takahashi 2010 climatology based on $f\text{CO}_{2w}$ data from
663 1985-2018 can be found as part of the RECCAP2 holdings at: Müller, J.D.
664 <https://doi.org/10.5281/zenodo.7990823>, Zenodo. The fluxes of the AOML_ET approach with
665 different input variables are stored at NCEI. [links provided at acceptance]

666

667 **References**

668 Bakker, D. C. E., Pfeil, B., Landa, C. S., Metzl, N., O'Brien, K. M., Olsen, A., et al. (2016). A
669 multi-decade record of high-quality $f\text{CO}_2$ data in version 3 of the Surface Ocean CO_2 Atlas
670 (SOCAT). *Earth Syst. Sci. Data* 8, 383-413. <http://www.earth-syst-sci-data.net/8/383/2016/>

671
672 Bennington, V., Galjanic, T., & McKinley, G. A. (2022). Explicit Physical Knowledge in
673 Machine Learning for Ocean Carbon Flux Reconstruction: The $p\text{CO}_2$ -Residual Method. *Journal*
674 *of Advances in Modeling Earth Systems*, 14(10), <https://doi.org/10.1029/2021MS002960>.

675
676 Bryan, K., & Lewis, L. J. (1979). A water mass model of the World Ocean. *Journal of*
677 *Geophysical Research: Oceans*, 84(C5), 2503-2517. <https://doi.org/10.1029/JC084iC05p02503>.

678
679 Bushinsky, S. M., Landschützer, P., Rödenbeck, C., Gray, A. R., Baker, D., Mazloff, M. R., et al.
680 (2019). Reassessing Southern Ocean air-sea CO_2 flux estimates with the addition of
681 biogeochemical float observations. *Global Biogeochemical Cycles*, 33(11), 1370-1388.
682 <https://agupubs.onlinelibrary.wiley.com/doi/abs/10.1029/2019GB006176>

683 Chau, T. T. T., Gehlen, M., & Chevallier, F. (2022). A seamless ensemble-based reconstruction
684 of surface ocean $p\text{CO}_2$ and air-sea CO_2 fluxes over the global coastal and open oceans.
685 *Biogeosciences*, 19(4), 1087-1109. <https://bg.copernicus.org/articles/19/1087/2022/>

686
687 DeVries, T., Yamamoto, K., Wanninkhof, R., Gruber, N., Hauck, J., Müller, J. D., et al. (2023).
688 Magnitude, trends, and variability of the global ocean carbon sink from 1985-2018. *Global*
689 *Biogeochemical Cycles*, e2023GB007780. <https://doi.org/10.1029/2023GB007780>

690
691 Dlugokencky, E.J., Thoning, K.W., Lan, X. & Tans, P.P. (2021). NOAA Greenhouse Gas
692 Reference from Atmospheric Carbon Dioxide Dry Air Mole Fractions from the NOAA GML
693 Carbon Cycle Cooperative Global Air Sampling Network.
694 Data Path: https://gml.noaa.gov/aftp/data/trace_gases/co2/flask/surface/.

695
696 Doney, S. C., Busch, D. S., Cooley, S. R., & Kroeker, K. J. (2020). The impacts of ocean
697 acidification on marine ecosystems and reliant human communities. *Annual Review of*
698 *Environment and Resources*, 45(1), 83-112. [https://doi.org/10.1146/annurev-environ-012320-](https://doi.org/10.1146/annurev-environ-012320-083019)
699 [083019](https://doi.org/10.1146/annurev-environ-012320-083019)

700
701 Fay, A. R., & McKinley, G. A. (2013). Global trends in surface ocean $p\text{CO}_2$ from in situ data.
702 *Global Biogeochemical Cycles*, 27(2), 541-557. <https://doi.org/10.1002/gbc.20051>

703
704 Fay, A. R., & McKinley, G. A. (2014). Global open-ocean biomes: mean and temporal
705 variability. *Earth Syst. Sci. Data*, 6(2), 273-284. <http://www.earth-syst-sci-data.net/6/273/2014/>

706

- 707 Fay, A. R., Gregor, L., Landschützer, P., McKinley, G. A., Gruber, N., Gehlen, M., et al. (2021).
708 SeaFlux: harmonization of air–sea CO₂ fluxes from surface pCO₂ data products using a
709 standardized approach. *Earth Syst. Sci. Data*, *13*(10), 4693–4710.
710 <https://essd.copernicus.org/articles/13/4693/2021/>
711
- 712 Fay, A. R., Munro, D. R., McKinley, G., Pierrot, D., Sutherland, S., Sweeney, C., &
713 Wanninkhof, R. (2023). Updated climatological mean delta fCO₂ and net sea–air CO₂ flux over
714 the global open ocean regions. *Earth System Science Data*, *submitted*.
715
- 716 Friedlingstein, P., Jones, M. W., O'Sullivan, M., Andrew, R. M., Bakker, D. C. E., Hauck, J., et
717 al. (2022). Global Carbon Budget 2021. *Earth System Science. Data*, *14*(4), 1917–2005.
718 <https://essd.copernicus.org/articles/14/1917/2022/>
719
- 720 Gregor, L., Lebehot, A. D., Kok, S., & Scheel Monteiro, P. M. (2019). A comparative
721 assessment of the uncertainties of global surface ocean CO₂ estimates using a machine-learning
722 ensemble (CSIR-ML6 version 2019a) – have we hit the wall? *Geosci. Model Dev.*, *12*(12), 5113–
723 5136. <https://gmd.copernicus.org/articles/12/5113/2019/>
724
- 725 Gregor, L., & Gruber, N. (2021). OceanSODA-ETHZ: a global gridded data set of the surface
726 ocean carbonate system for seasonal to decadal studies of ocean acidification. *Earth Syst. Sci.*
727 *Data*, *13*(2), 777–808. <https://essd.copernicus.org/articles/13/777/2021/>
728
729
- 730 Geurts, P., Ernst, D., & Wehenkel, L. (2006). Extremely randomized trees. *Machine Learning*,
731 *63*(1), 3–42. <https://doi.org/10.1007/s10994-006-6226-1>
732
- 733 Gray, A. R., Johnson, K. S., Bushinsky, S. M., Riser, S. C., Russell, J. L., Talley, L. D., et al.
734 (2018). Autonomous biogeochemical floats detect significant carbon dioxide outgassing in the
735 high-latitude Southern Ocean. *Geophys. Res. Lett.* <http://dx.doi.org/10.1029/2018GL078013>
736
- 737 Hauck, J., C. Nissen, P. Landschützer, C. Rödenbeck, S. Bushinsky, and A. Olsen (2023), Sparse
738 observations induce large biases in estimates of the global ocean CO₂ sink: an ocean model
739 subsampling experiment, *Philosophical Transactions of the Royal Society A: Mathematical,*
740 *Physical and Engineering Sciences*, *381*(2249), 20220063, doi:10.1098/rsta.2022.0063.
741
- 742 Hersbach, H., Bell, B., Berrisford, P., Hirahara, S., Horányi, A., Muñoz-Sabater, J., et al. (2020).
743 The ERA5 global reanalysis. *Quarterly Journal of the Royal Meteorological Society*, *146*(730),
744 1999–2049. <https://doi.org/10.1002/qj.3803>.
745
- 746 IPCC, 2018: Annex I: Glossary [Matthews, J.B.R. (ed.)]. In: *Global Warming of 1.5°C. An IPCC*
747 *Special Report on the impacts of global warming of 1.5°C above pre-industrial levels and*
748 *related global greenhouse gas emission pathways, in the context of strengthening the global*
749 *response to the threat of climate change, sustainable development, and efforts to eradicate*
750 *poverty* [Masson-Delmotte, V., P. Zhai, H.-O. Pörtner, D. Roberts, J. Skea, P.R. Shukla, A.
751 Pirani, W. Moufouma-Okia, C. Péan, R. Pidcock, S. Connors, J.B.R. Matthews, Y. Chen, X.
752 Zhou, M.I. Gomis, E. Lonnoy, T. Maycock, M. Tignor, and T. Waterfield (eds.)]. Cambridge

- 753 University Press, Cambridge, UK and New York, NY, USA, pp. 541-562,
754 <https://doi.org/10.1017/9781009157940.008>.
- 755
- 756 Jacobson, A. R., et al. (2020), CarbonTracker CT2019B, edited, NOAA Global Monitoring
757 Laboratory, <https://doi.org/10.25925/20201008>.
- 758
- 759 Krol, M., Houweling, S., Bregman, B., van den Broek, M., Segers, A., van Velthoven, P., et al.
760 (2005). The two-way nested global chemistry-transport zoom model TM5: algorithm and
761 applications. *Atmos. Chem. Phys.*, 5(2), 417-432. <https://acp.copernicus.org/articles/5/417/2005/>.
- 762
- 763 Landschützer, P., Gruber, N., Bakker, D. C. E., Schuster, U., Nakaoka, S., Payne, M. R., et al.
764 (2013). A neural network-based estimate of the seasonal to inter-annual variability of the
765 Atlantic Ocean carbon sink. *Biogeosciences*, 10(11), 7793-7815.
766 <http://www.biogeosciences.net/10/7793/2013/>
- 767
- 768 Landschützer, P., Gruber, N., & Bakker, D. C. E. (2016). Decadal variations and trends of the
769 global ocean carbon sink. *Global Biogeochemical Cycles*, 30(10), 1396-1417.
770 <https://doi.org/10.1002/2015GB005359>.
- 771
- 772 Landschützer, P., Gruber, N., Bakker, D. C. E., Stemmler, I., & Six, K. D. (2018). Strengthening
773 seasonal marine CO₂ variations due to increasing atmospheric CO₂. *Nature Climate Change*.
774 <https://doi.org/10.1038/s41558-017-0057-x>
- 775
- 776 Li, Z., Adamec, D., Takahashi, T., & Sutherland, S. C. (2005). Global autocorrelation scales of
777 the partial pressure of oceanic CO₂. *Journal of Geophysical Research: Oceans*, 110(C8).
778 <https://doi.org/10.1029/2004JC002723>.
- 779
- 780 Lida, Y., Takatani, Y., Kojima, A., & Ishii, M. (2021). Global trends of ocean CO₂ sink and
781 ocean acidification: an observation-based reconstruction of surface ocean inorganic carbon
782 variables. *J. Oceanogr.*, 77, 323-358.
- 783
- 784 Magnan, A. K., Colombier, M., Bille, R., Joos, F., Hoegh-Guldberg, O., Portner, H.-O., et al.
785 (2016). Implications of the Paris agreement for the ocean. *Nature Clim. Change, advance online*
786 *publication*. Commentary. <http://dx.doi.org/10.1038/nclimate3038>
- 787
- 788 McKinley, G. A., Fay, A. R., Eddebbar, Y. A., Gloege, L., & Lovenduski, N. S. (2020). External
789 forcing explains recent decadal variability of the ocean carbon sink. *AGU Advances*, 1(2),
790 e2019AV000149. <https://doi.org/10.1029/2019AV000149>.
- 791
- 792 Müller, J. D. (2023). RECCAP2-ocean data collection [Version V1].
793 <https://doi.org/10.5281/zenodo.7990823>, Zenodo
- 794
- 795 Northcott, D., Sevadjan, J., Sancho-Gallegos, D. A., Wahl, C., Friederich, J., & Chavez, F. P.
796 (2019). Impacts of urban carbon dioxide emissions on sea-air flux and ocean acidification in
797 nearshore waters. *PLoS ONE*, 14(3), e0214403. <https://doi.org/10.1371/journal.pone.0214403>
- 798

- 799 Palter, J. B., Nickford, S., & Mu, L. (2023). Ocean carbon dioxide uptake in the tailpipe of
800 industrialized continents. *Geophysical Research Letters*, *accepted*.
801
- 802 Pierrot, D., Neil, C., Sullivan, K., Castle, R., Wanninkhof, R., Lueger, H., et al. (2009).
803 Recommendations for autonomous underway pCO₂ measuring systems and data reduction
804 routines. *Deep -Sea Res II*, *56*, 512-522.
805
- 806 Rödenbeck, C., D. C. E. Bakker, N. Gruber, Y. Iida, A. R. Jacobson, S. Jones, et al. (2015).
807 Data-based estimates of the ocean carbon sink variability –first results of the Surface Ocean
808 pCO₂ Mapping intercomparison (SOCOM). *Biogeosciences*, *12*, 7251-7278.
809
- 810 Rödenbeck, C., DeVries, T., Hauck, J., Le Quéré, C., & Keeling, R. F. (2022). Data-based
811 estimates of interannual sea–air CO₂ flux variations 1957–2020 and their relation to
812 environmental drivers. *Biogeosciences*, *19*(10), 2627-2652.
813 <https://bg.copernicus.org/articles/19/2627/2022/>
814
- 815 Roobaert, A., Laruelle, G. G., Landschützer, P., & Regnier, P. (2018). Uncertainty in the global
816 oceanic CO₂ uptake induced by wind forcing: quantification and spatial analysis.
817 *Biogeosciences*, *15*(6), 1701-1720. <https://www.biogeosciences.net/15/1701/2018/>
818
- 819 Stamell, J., Rustagi, R. R., Gloege, L., & McKinley, G. A. (2020). Strengths and weaknesses of
820 three Machine Learning methods for pCO₂ interpolation. *Geosci. Model Dev. Discuss.*, *2020*, 1-
821 25. <https://gmd.copernicus.org/preprints/gmd-2020-311/>
822
- 823 Sweeney, C., Gloor, E., Jacobson, A. R., Key, R. M., McKinley, G., Sarmiento, J. L., &
824 Wanninkhof, R. (2007). Constraining global air-sea gas exchange for CO₂ with recent bomb C-
825 14 measurements. *Global Biogeochem. Cycles*, *21*(2), GB2015.
826
- 827 Takahashi, T., Feely, R. A., Weiss, R., Wanninkhof, R., Chipman, D. W., Sutherland, S. C., &
828 Takahashi, T. T. (1997). Global air-sea flux of CO₂: An estimate based on measurements of sea-
829 air pCO₂ difference. *Proc. Natl. Acad. Sci. USA*, *94*, 8292-8299.
830
- 831 Takahashi, T., Sutherland, S. C., Wanninkhof, R., Sweeney, C., Feely, R. A., Chipman, D. W., et
832 al. (2009). Climatological mean and decadal change in surface ocean pCO₂, and net sea-air CO₂
833 flux over the global oceans. *Deep -Sea Res II*, *2009*, 554-577.
834
- 835 Telszewski, M., Chazottes, A., Schuster, U., Watson, A. J., Moulin, C., Bakker, D. C. E., et al.
836 (2009). Estimating the monthly pCO₂ distribution in the North Atlantic using a self-organizing
837 neural network. *Biogeosciences*, *6*, 1405-1421.
838
- 839 Wanninkhof, R., Doney, S. C., Takahashi, T., & McGillis, W. R. (2002). The effect of using
840 time-averaged winds on regional air-sea CO₂ fluxes. In M. Donelan, W. Drennan, E. Saltzman,
841 & R. Wanninkhof (Eds.), *Gas Transfer at Water Surfaces*. Geophysical Monograph 127, pp.
842 351-357. Washington, DC: AGU, Geophysical Monograph 127.
843

844 Wanninkhof, R., Asher, W. E., Ho, D. T., Sweeney, C. S., & McGillis, W. R. (2009). Advances
845 in quantifying air-sea gas exchange and environmental forcing. *Annual Reviews Mar. Science, 1*,
846 213-244,.

847
848 Wanninkhof, R., Park, G.-H., Chelton, D., & Resien, C. (2011). Impact of small-scale variability
849 on air-sea CO₂ fluxes. In S. Komori, W. McGillis, & R. Kurose (Eds.), *Gas transfer at water*
850 *surfaces 2010* (pp. 431-444). Kyoto: Kyoto University Press.

851
852 Wanninkhof, R., Bakker, D., Bates, N., Olsen, A., & Steinhoff, T. (2013). Incorporation of
853 alternative sensors in the SOCAT database and adjustments to dataset quality control flags.
854 Retrieved from Oak Ridge, Tennessee: https://doi.org/10.3334/CDIAC/OTG.SOCAT_ADQCF

855
856 Wanninkhof, R. (2014), Relationship between wind speed and gas exchange over the ocean
857 revisited, *Limnol and Oceanogr: Methods, 12*, 351-362,
858 <https://doi.org/10.4319/lom.2014.12.351>.

859
860 Wanninkhof, R., Pickers, P. A., Omar, A. M., Sutton, A., Murata, A., Olsen, A., et al. (2019). A
861 Surface Ocean CO₂ Reference Network, SOCONET and Associated Marine Boundary Layer
862 CO₂ Measurements. *Frontiers in Marine Science, 6*, 400. [10.3389/fmars.2019.00400](https://doi.org/10.3389/fmars.2019.00400).
863 <https://www.frontiersin.org/article/10.3389/fmars.2019.00400>

864
865 Wanninkhof, R., Pierrot, D., Sullivan, K., Mears, P., & Barbero, L. (2022). Comparison of
866 discrete and underway CO₂ measurements: Inferences on the temperature dependence of the
867 fugacity of CO₂ in seawater. *Marine Chemistry, 247*, 104178.
868 <https://www.sciencedirect.com/science/article/pii/S0304420322000950>

869
870 Watson, A. J., Schuster, U., Shutler, J. D., Holding, T., Ashton, I. G. C., Landschützer, P., et al.
871 (2020). Revised estimates of ocean-atmosphere CO₂ flux are consistent with ocean carbon
872 inventory. *Nature Communications, 11*(1), 4422. <https://doi.org/10.1038/s41467-020-18203-3>

873
874
875 Weiss, R. F., & Price, B. A. (1980). Nitrous oxide solubility in water and seawater. *Mar. Chem.*,
876 *8*, 347-359. [https://doi.org/10.1016/0304-4203\(80\)90024-9](https://doi.org/10.1016/0304-4203(80)90024-9).

877
878 Zeng, J., Nojiri, Y., Landschützer, P., Telszewski, M., & Nakaoka, S. (2014). A Global Surface
879 Ocean fCO₂ Climatology Based on a Feed-Forward Neural Network. *Journal of Atmospheric*
880 *and Oceanic Technology, 31*, 1838-1849. doi:<https://doi.org/10.1175/JTECH-D-13-00137.1>.

881 **Appendix:**

882
883
884 The default configurations of the ET sea-air CO₂ flux product, AOML_EXTRAT, submitted to
885 RECCAP2, was produced to meet the RECCAP2 requirements and nomenclature. The output
886 provided for RECCAP2 are pCO₂ values on a 1° by 1° monthly grid. The details of the predictor
887 and target variables, units, and nomenclature as prescribed by RECCAP2, and those used
888 AOML_EXTRAT_1998-2020 are provided in Table A1. If the AOML_ET parameters are
889 different than specified in RECCAP2 they are added in italics.

890

891 **Appendix Table A1**

892 <i>Creation of pCO₂ maps</i>				
893 Variables¹	abbrev.	unit	Source/notes	
894 Training set				
895 Partial pressure of CO ₂	spCO ₂	µatm	monthly gridded data SOCATv2020 ²	
896 <i>Fugacity of CO₂</i>	fCO _{2w}	µatm	SOCAT v2020 ³	
897 Sea surface temperature	SST	°C	gridded data SOCAT v2020	
898 Sea surface salinity	SSS		gridded data SOCAT v2020	
899 Mixed layer depth	MLD		HYCOM model ⁴	
900 Julian day	JDN	mo	month since Oct. 1997	
901 Latitude	LAT	degree		
902 Longitude	SLON	degree	vector longitude (SIN)	
903 Longitude	CLON	degree	vector longitude (COS)	
904 Chlorophyll-a	Chl-a	log (mg/l)	oceancolor.gsfc.nasa.gov	
905				
906 Dependent variable/ Target				
907 Partial pressure of CO ₂	spCO ₂	µatm	for surface water	
908 <i>Fugacity of CO₂</i>	fCO _{2w}	µatm	for surface water	
909				
910 Predictor/Interpolation variable				
911 Sea surface temperature	STT	°C	NOAA OISST	
912 Sea surface salinity	SSS		HYCOM	
913 Mixed layer depth	MLD	m	HYCOM	
914 Chlorophyll-a	Chl-a	log (mg/l)	oceancolor.gsfc.nasa.gov ⁵	
915 Julian day	JDN	mo	month since Oct. 1997	
916 Latitude	Lat			
917 Longitude	SLON		vector longitude (SIN)	
918 Longitude	CLON		vector longitude (COS)	
919				
920 <i>Determination of flux maps</i>				
921 Dependent variable				
922 Sea-air CO ₂ flux density	F _{sa}	mol m ⁻² s ⁻¹	F _{sa} = k K ₀ (1-f _{ice}) (pCO _{2atm} -spCO ₂)	
923 <i>Sea-air CO₂ flux density</i>	F _{sa}	mol m ⁻² y ⁻¹	F _{sa} = k K ₀ (1-f _{ice}) (fCO _{2w} -fCO _{2a})	
924 Sea-air piston velocity K _w		m s ⁻¹	Wanninkhof (1992, 2014)	
925 <i>Gas transfer velocity</i>	k	cm hr ⁻¹	Wanninkhof (2014)	
926 Schmidt number	Sc		Wanninkhof (2014)	
927 Second moment wind	<u ² >	m ² s ⁻²	ERA5 wind ⁶	
928 Solubility	alpha	mol kg ⁻¹ atm ⁻¹	Weiss and Price (1980)	
929 <i>Solubility</i>	K ₀	mol l ⁻¹ atm ⁻¹	Weiss and Price (1980)	
930 <i>Ice cover</i>	f _{ice}	fraction	NOAA OISST ⁷	
931 Water partial pressure	spCO ₂	µatm	SOCAT	
932 <i>Water fugacity of CO₂</i>	fCO ₂	µatm	SOCATV2020	
933 Air partial pressure	pCO _{2atm} ⁸	µatm	zonal mo. average xCO ₂ MBL-RS	
934 <i>Air fugacity of CO₂</i>	fCO _{2a} ⁹	µatm	zonal mo. average xCO ₂ MBL-RS	
935 Partial pres. difference	ΔpCO ₂	µatm	pCO _{2atm} - spCO ₂	
936 <i>Air-water fugacity difference</i>	ΔfCO ₂	µatm	fCO _{2w} -fCO _{2a}	

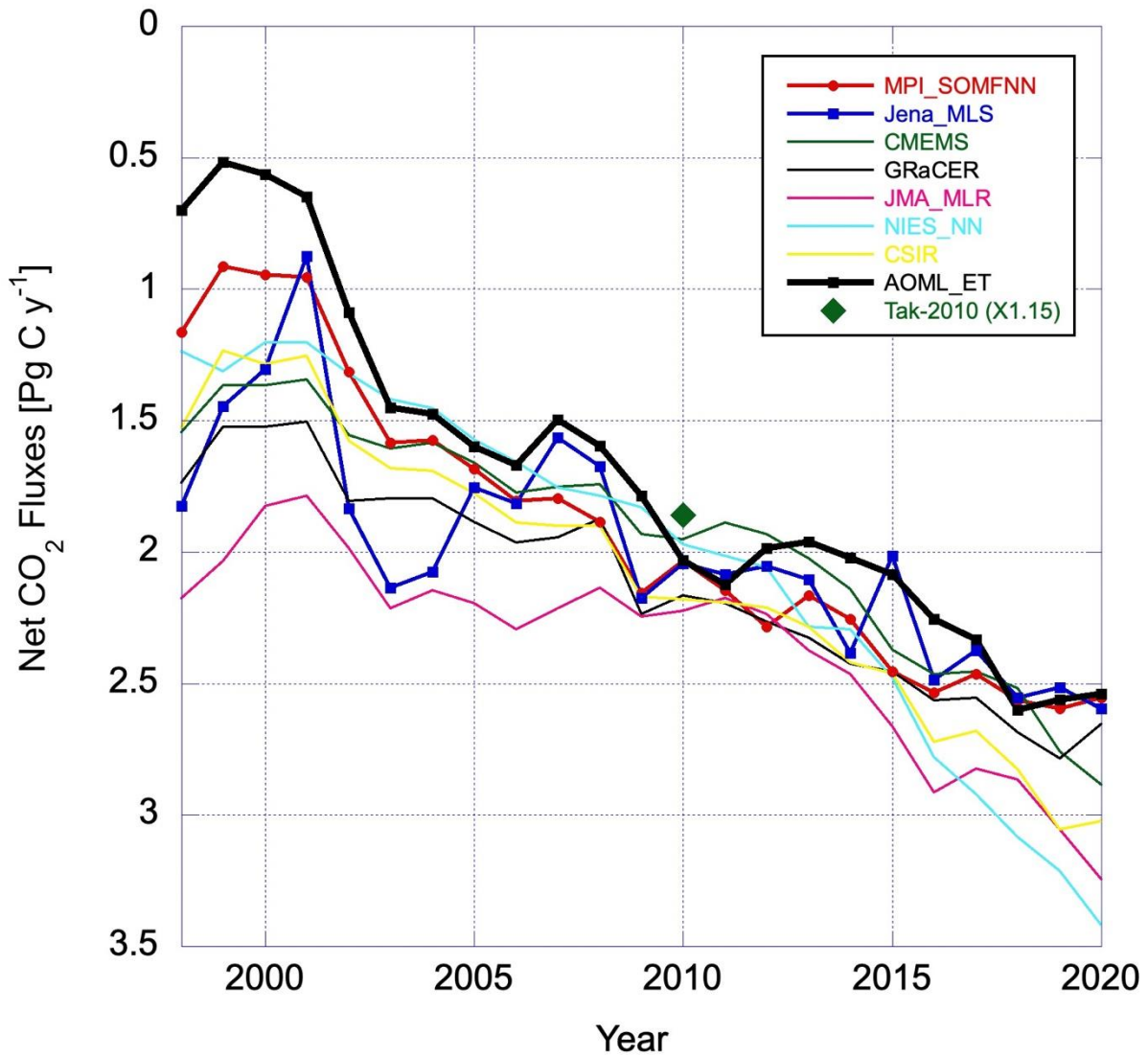
937	Global Flux	fgco2_glob	Pg C y ⁻¹	Efflux negative in RECCAP2
938	<i>Flux</i>	F	Pg C y ⁻¹	Efflux positive

939

- 940 1. Extra Trees (ET) regressors used to estimate the $\text{spCO}_2/\text{fCO}_{2\text{w}}$ values are: date, location, sea
 941 surface temperature, sea surface salinity, mixed-layer depth, and chlorophyll concentration.
- 942 2. SOCAT data are converted from fCO_2 to pCO_2 to meet the RECCAP2 submission criteria.
 943 These are gridded products based on the monthly 1° by 1° gridded SOCATv2020 data
 944 holdings using datasets with QC flags of A through D, and SOCAT data points flagged with
 945 WOCE flag values of 2. See,
 946 [https://www.ncei.noaa.gov/data/oceans/ncei/ocads/data/0210711/
 947 SOCATv2020_Gridded_Dat/SOCATv2020_tracks_gridded_monthly.nc](https://www.ncei.noaa.gov/data/oceans/ncei/ocads/data/0210711/SOCATv2020_Gridded_Dat/SOCATv2020_tracks_gridded_monthly.nc). The submission to
 948 RECCAP2 for the time period October 1997- December 2018 uses data from SOCATv2020
 949 while the analysis in this paper uses SOCATv2021 and covers the time period October 1997-
 950 December 2020.
- 951 3. Two Different SOCATv2020 products are used in our analyses, the first is the default (see
 952 footnote 2) and a product using only datasets labeled A and B with accuracies better than 2
 953 μatm (compared to 5 μatm in the full dataset).
- 954 4. Mixed layer depth is based on a criteria of 0.03 change in density and provided in
 955 <http://orca.science.oregonstate.edu/2160.by.4320.monthly.hdf.mld030.hycom.php>
- 956 5. Chl-a are from the NASA Ocean color Monthly Fields from SeaWiFS, and AQUA/TERRA-
 957 MODIS from: <https://oceancolor.gsfc.nasa.gov/>.
- 958 6. From <https://www.ecmwf.int/en/forecasts/datasets/reanalysis-datasets/era5> where the 6-hourly
 959 winds are aggregated on the monthly 1° by 1° grid to produce the second and third moments
 960 of the wind, $\langle u^2 \rangle$, and $\langle u^3 \rangle$.
- 961 7. From <ftp://ftp.cdc.noaa.gov/Datasets/noaa.oisst.v2/icec.mnmean.nc> following the approach of
 962 Takahashi et al, (2005) where k is scaled by $(1-f)$ where f is the fraction of sea-ice covering
 963 the monthly 1° x 1° grid.
- 964 8. $\text{pCO}_{2\text{atm}} = P (1-\text{pH}_2\text{O}) \text{XCO}_{2\text{a}}$ where $\text{XCO}_{2\text{a}}$ is the interpolated MBL-RS product from
 965 NOAA/GML: https://www.esrl.noaa.gov/gmd/ccgg/mbl/mbl.html#ghg_product.
- 966 9. $\text{fCO}_{2\text{a}} = \text{Gf}(T,S) (P - \text{pH}_2\text{O}) \text{XCO}_{2\text{a}}$ where, $\text{Gf}(T,S)$ is the fugacity correction and pH_2O is the
 967 water vapor correction as summarized in Pierrot et al. (2009). P is the barometric pressure.

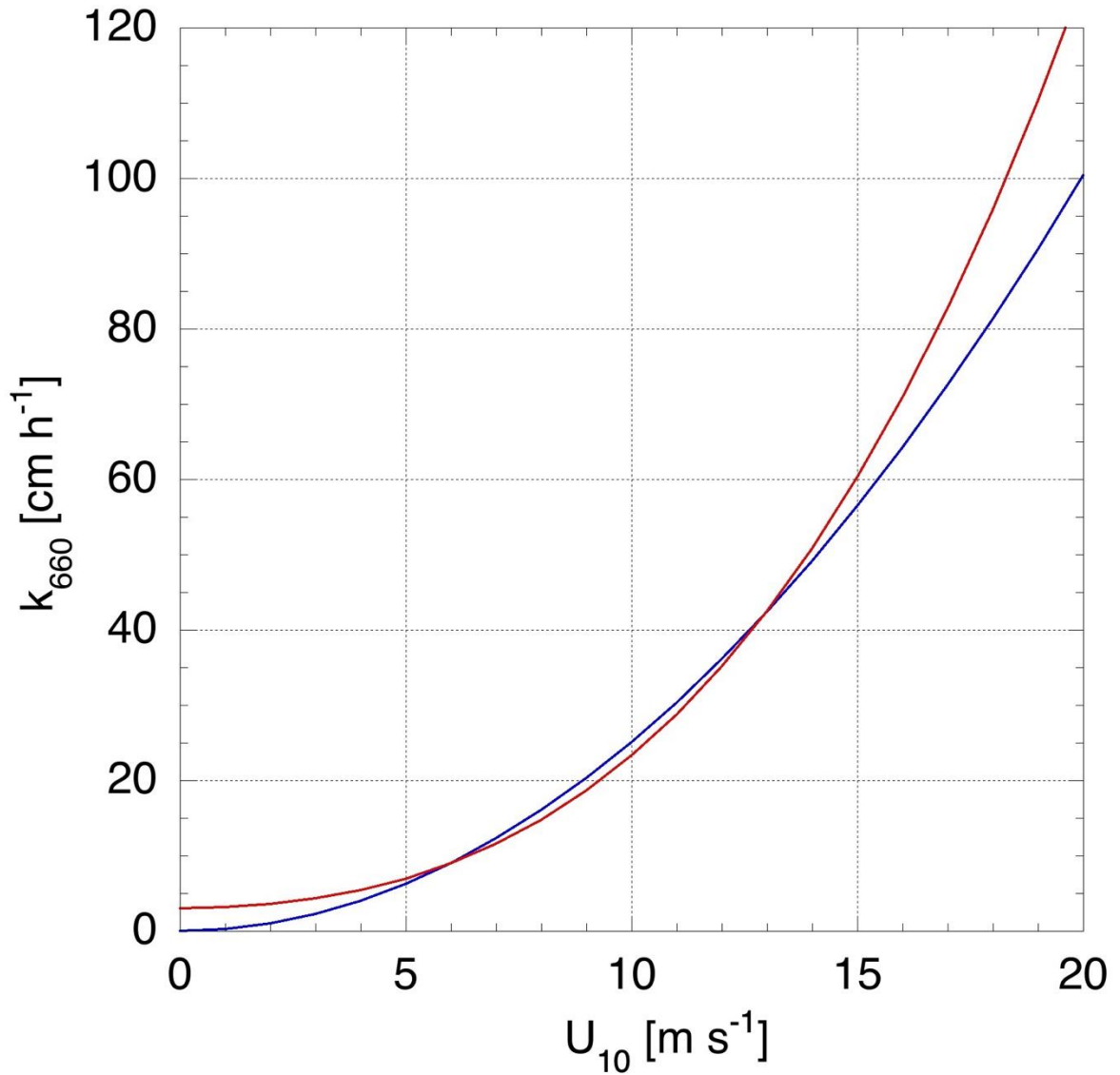
968

969 **Figures**

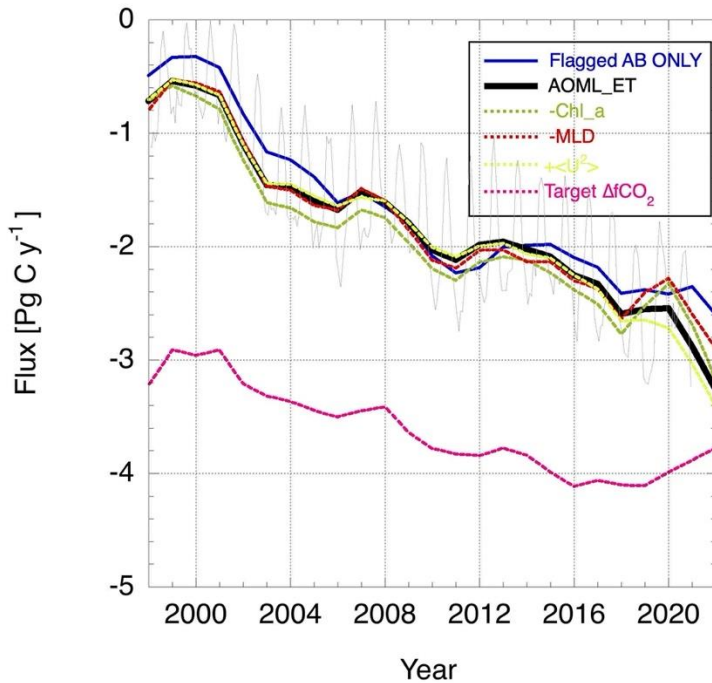


970
 971
 972
 973
 974
 975
 976

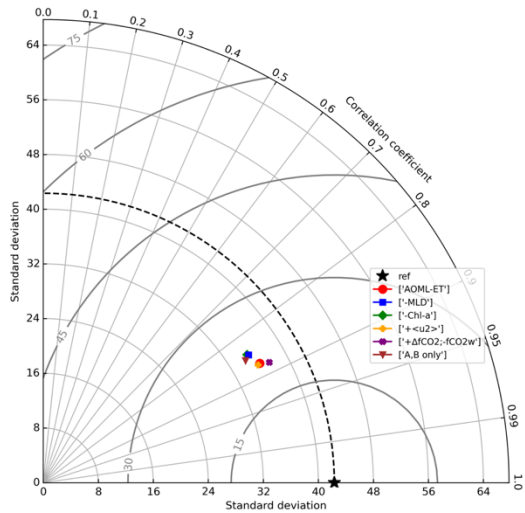
Figure 1. Global net air-sea CO₂ fluxes from 1998-2020 determined with a variety of ML and regression approaches. Data are from <https://globalcarbonbudgetdata.org/latest-data.html> [Global_Carbon_Budget_2022v1.0.xlsx] [0.65 Pg C is subtracted to get the net air-sea CO₂ flux]. For references of the methods see caption Table 1.



977
 978 Figure 2. The canonical dependence of gas transfer with the square of square the windspeed,
 979 $k_{660} = 0.251 \langle u^2 \rangle$ (blue line) and a hybrid dependence $k_{660} = 3 + 0.1 \langle u \rangle + 0.083 \langle u^2 \rangle +$
 980 $0.011 \langle u^3 \rangle$ meeting the same global uptake of bomb ^{14}C constraint. For wind between 5
 981 and 13 m s^{-1} the wind speed squared relationship will yield larger gas transfer
 982 velocities, outside this range the hybrid dependence yields greater fluxes.
 983



984

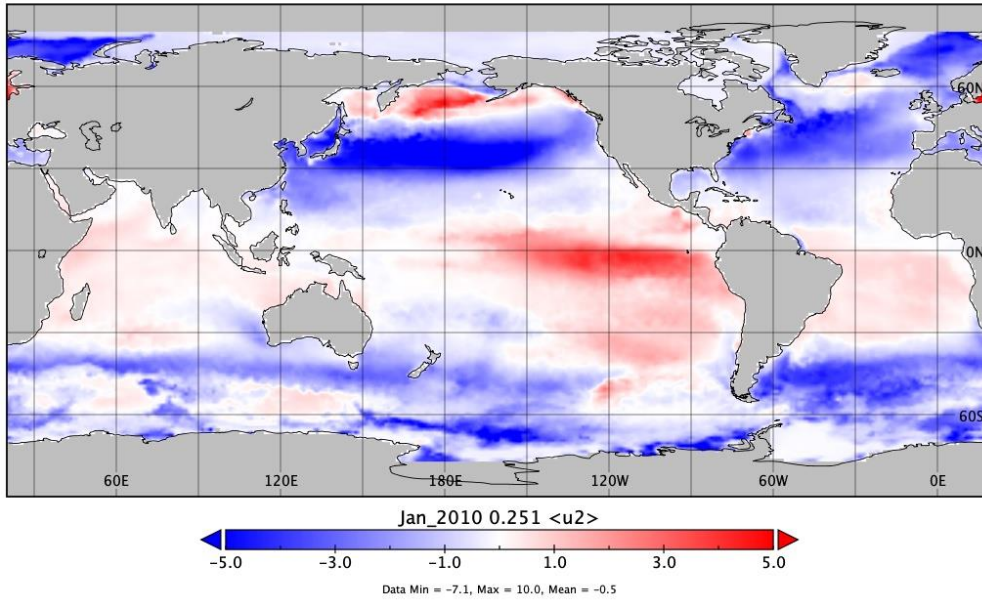


985

986

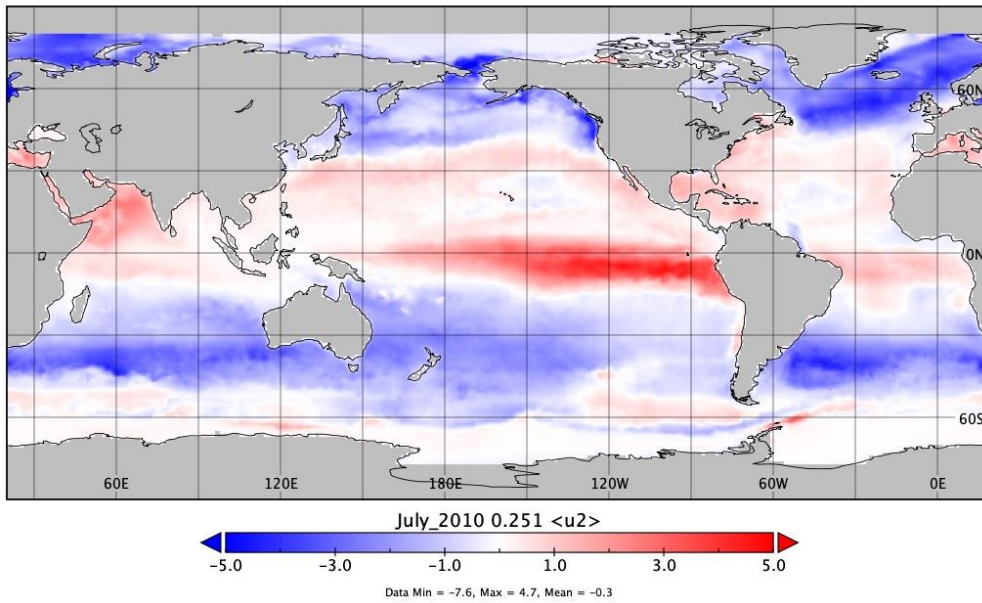
987 Figure 3. (a) Global net air-sea CO₂ fluxes from 1998-2020 using different predictor and target
 988 variables for the AOML_ET method. Black line: default AOML_ET; blue line:
 989 SOCAT data flagged A or B < 2 μatm only; green dashed line: omitting Chl-a as
 990 predictor; red dashed line: omitting MLD as predictor; yellow dashed line: including
 991 <u²> as predictor; and pink dashed line: using ΔfCO₂ instead of fCO_{2w} as target. The
 992 thin gray line shows the monthly variation in flux for AOML_ET (b) a Taylor diagram
 993 of the AOML_ET values for the permutations listed in a.
 994

Sea-air CO₂ flux



995
996
997

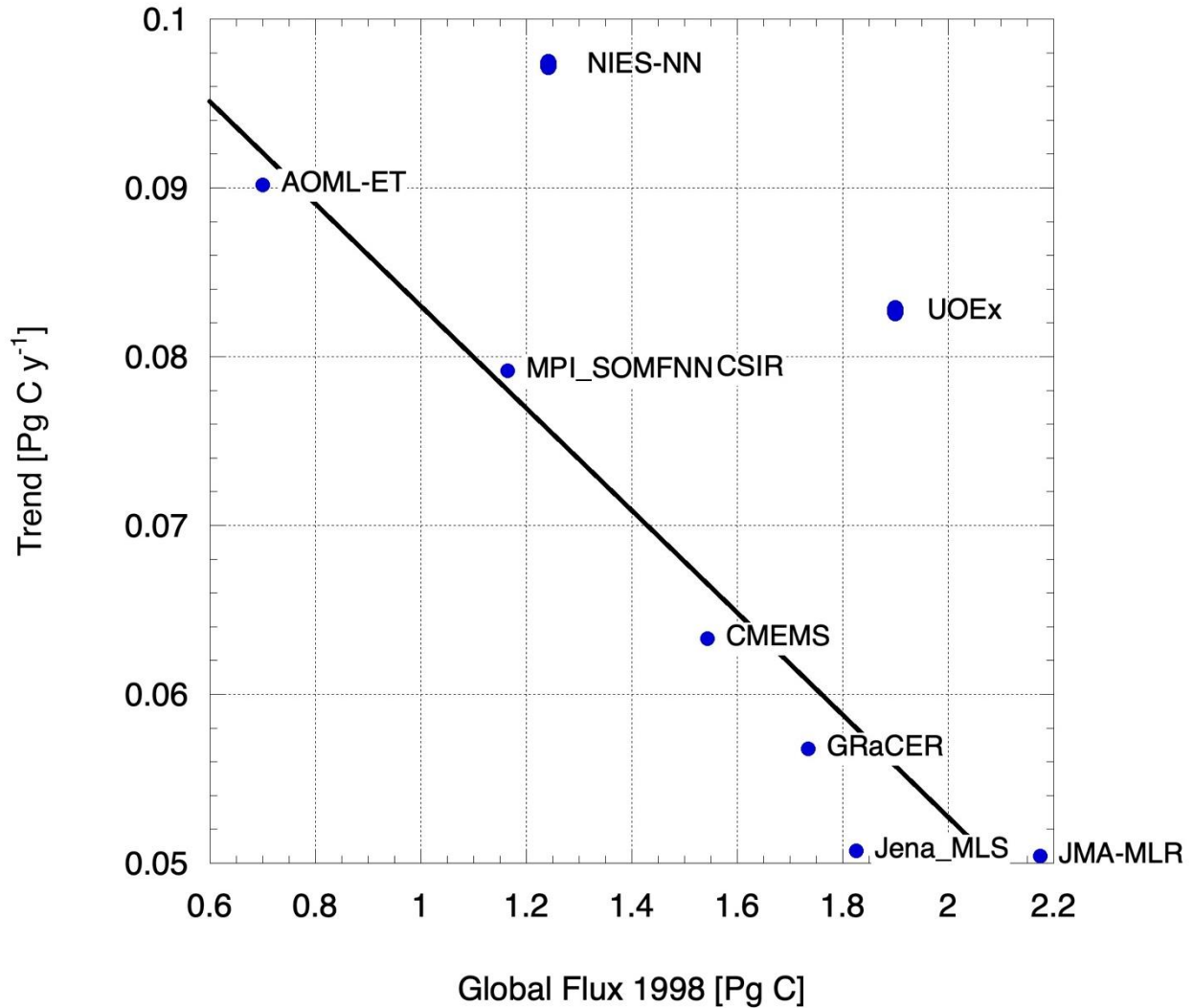
Sea-air CO₂ flux



998
999
1000
1001
1002
1003
1004
1005
1006

Figure 4. Flux maps for January (a) and July (b) 2010 using AOML_ET providing a visual depiction of spatial and seasonal changes for 2010. Color bar units [$\text{mol m}^{-2} \text{y}^{-1}$].

1007
 1008
 1009
 1010
 1011
 1012



1013
 1014
 1015
 1016
 1017
 1018

Figure 5. Relationship between global ocean CO₂ uptake in 1998 and trend from 1998 to 2020 for different ML methods. The linear relationship plotted ($\text{Trend [Pg C y}^{-1}] = 0.11 - 0.03 \text{ Flux}(1998)$ $R^2 = 0.84$) does not include the ML approaches of NIESS-NN and UoEx. For references of the methods see caption in Table 1.

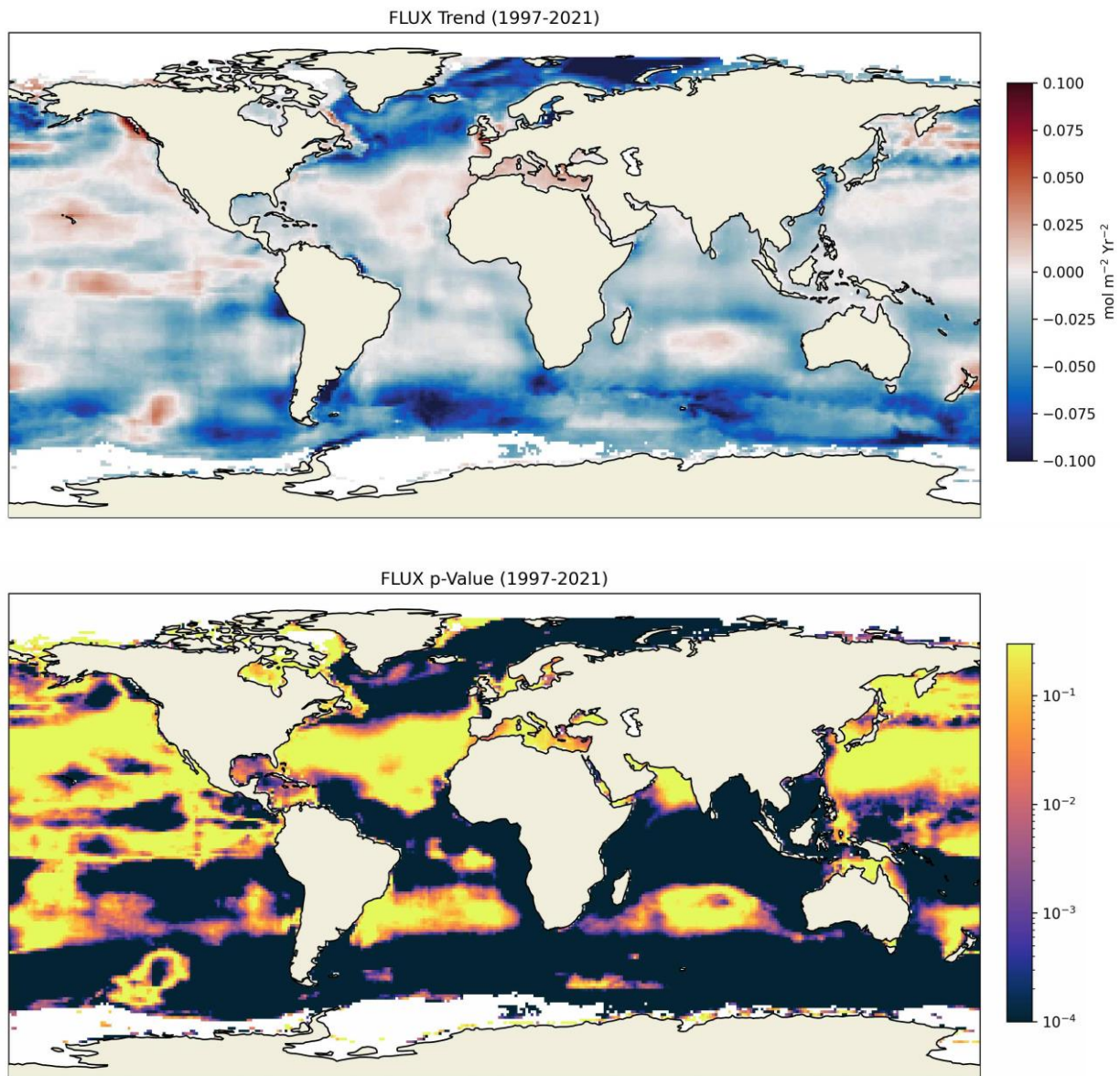
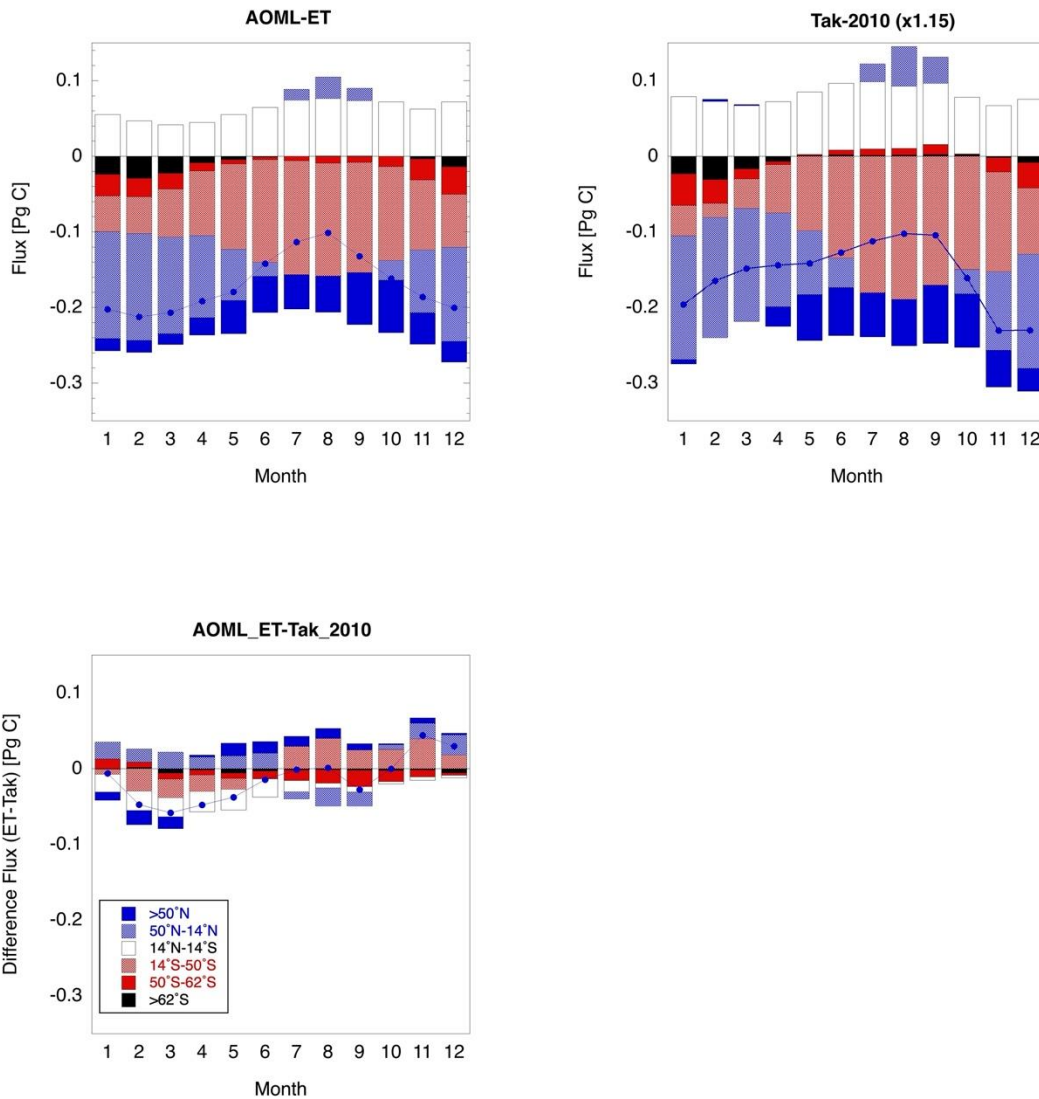
1019
10201021
10221023
1024
1025
1026
1027
1028
1029
1030
1031
1032
1033
1034
1035
1036

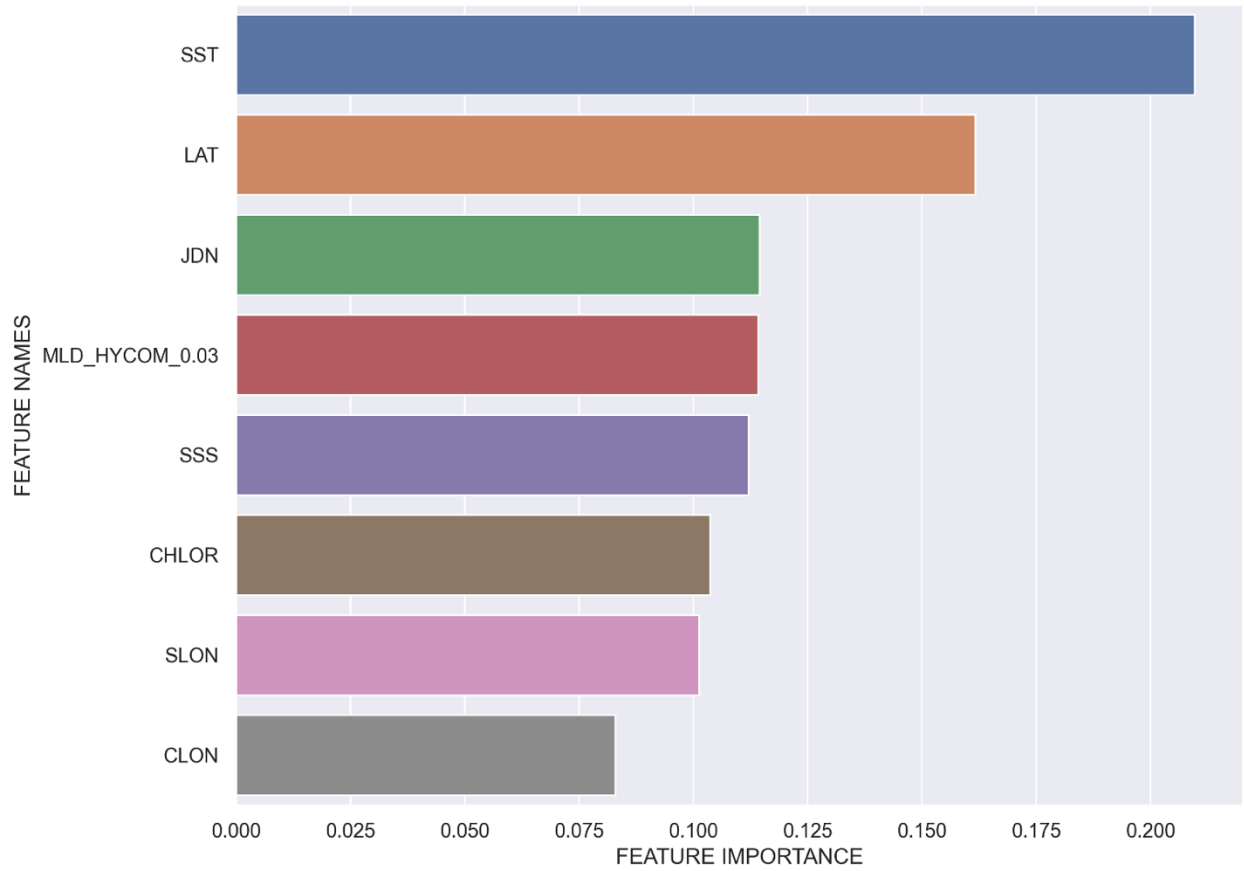
Figure 6. (a) Map of differing trends in sea-air CO₂ fluxes from 1998-2020 in mol m⁻² y⁻² and (b) P-values for trend for AOML_ET. The large trends both positive and negative have P values of less than 0.01 that are statistically significant.



1037
1038

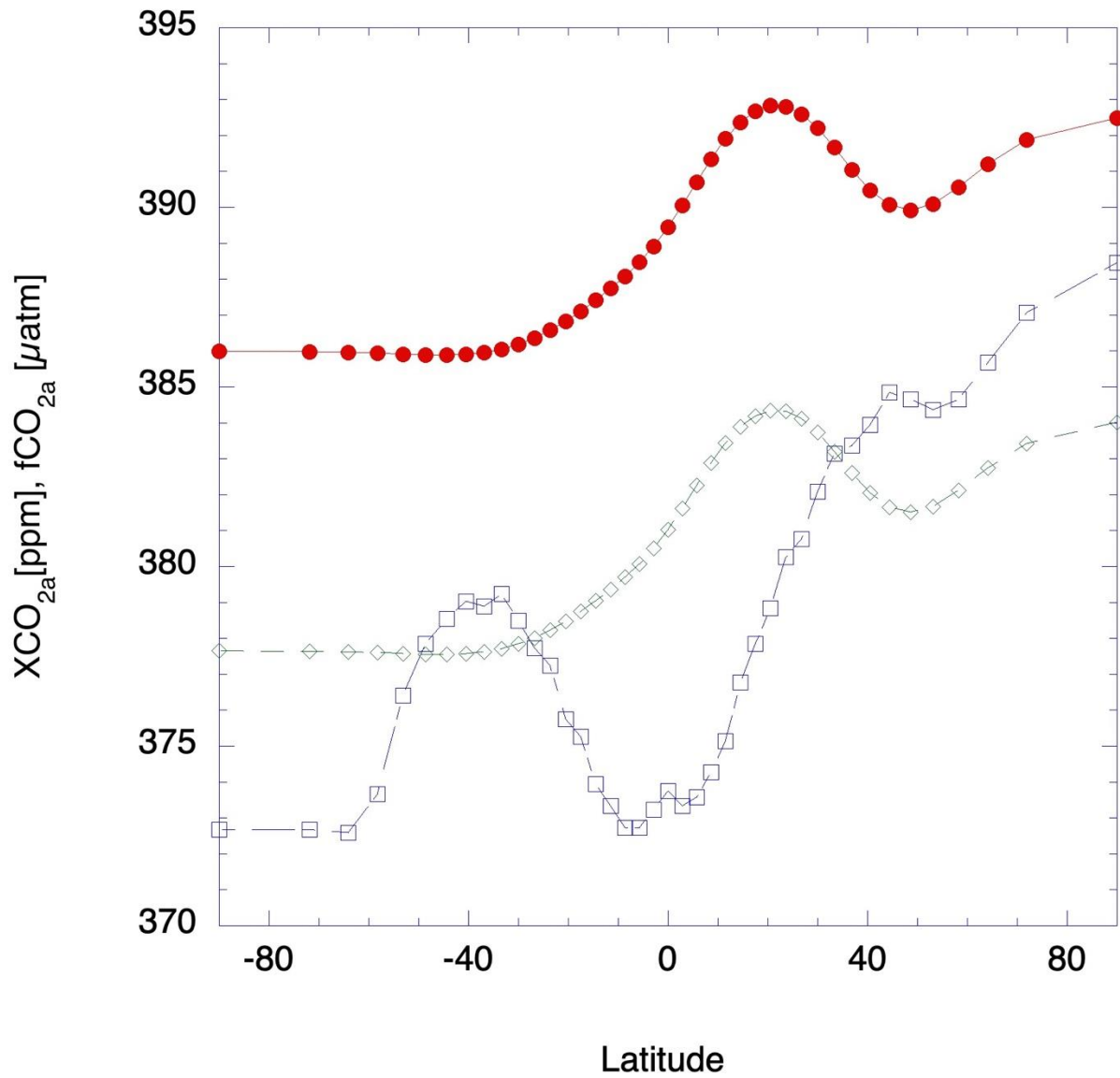
1039
1040
1041
1042
1043
1044
1045
1046

Figure 7. Regional monthly zonal fluxes based on the (a) AOML_ET effort; that of (b) Tak-2010, scaled to the same surface area (x1.15); and (c) the difference. The different zones following Takahashi et al. (2009) are listed in the legend. The lines with blue circles are the net monthly fluxes for 2010. Fluxes are expressed in [Pg C per month].



1047
 1048
 1049
 1050
 1051
 1052
 1053
 1054
 1055

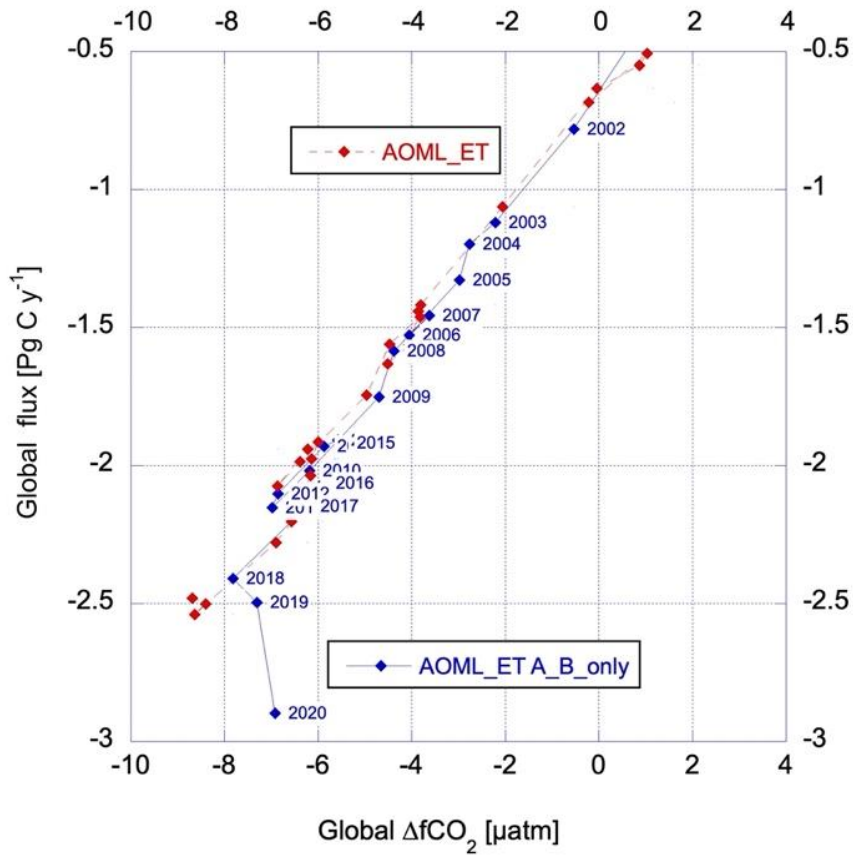
Figure 8. Importance of the different predictor variables in the AOML_ET analysis. Location (latitude (Lat), and longitude (SLON and CLON)) has the greater importance for predictability followed by SST. The other products, Julian day (JDN), Mixed layer depth (MLD-Hycom_0.03), sea surface salinity (SSS), and Chlorophyll-a (Chl-a) have similar impact.



1056
 1057
 1058
 1059
 1060

Figure 9. Zonal average XCO_{2a} (red line with circles); fCO_{2a} at fixed temperature of 16.1°C and pressure of 1 atm (dashed green line with diamonds); and fCO_{2a} at measured temperature and pressure (dashed blue line with squares) for June 2010.

1061



1062
 1063
 1064
 1065
 1066
 1067
 1068
 1069
 1070

Figure 10. Global net flux for the default AOML_ET approach using data sets flagged A-D (red line), and datasets A,B (blue line) versus global average $\Delta f\text{CO}_2$. The regression between net flux and $\Delta f\text{CO}_2$ is $0.214 \text{ Pg C}/\mu\text{atm}$, ($r^2 = 0.99$) for all data, and $0.227 \text{ Pg C}/\mu\text{atm}$, ($r^2 = 0.99$) for A, B data only, omitting the datapoint for 2020.

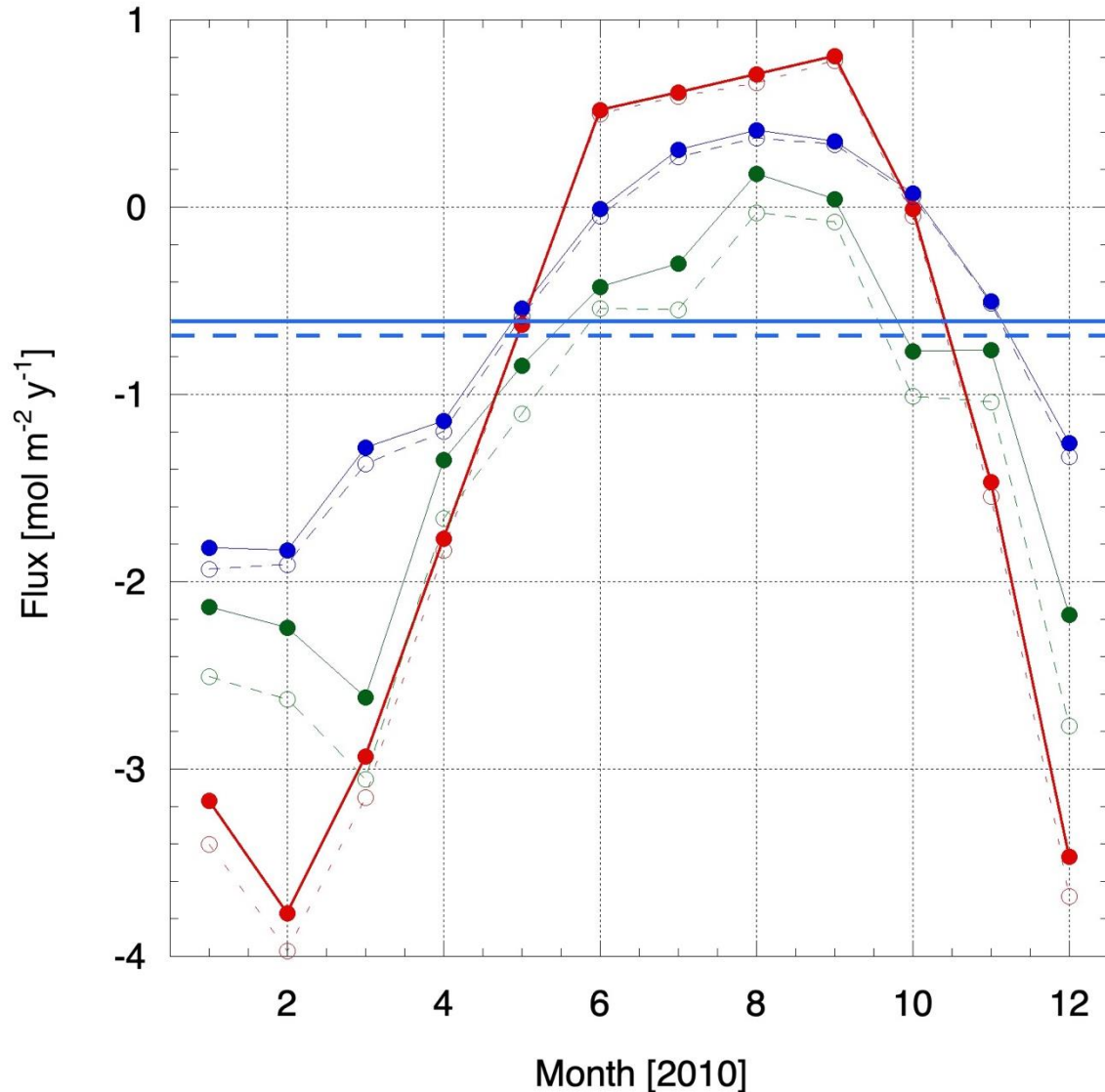
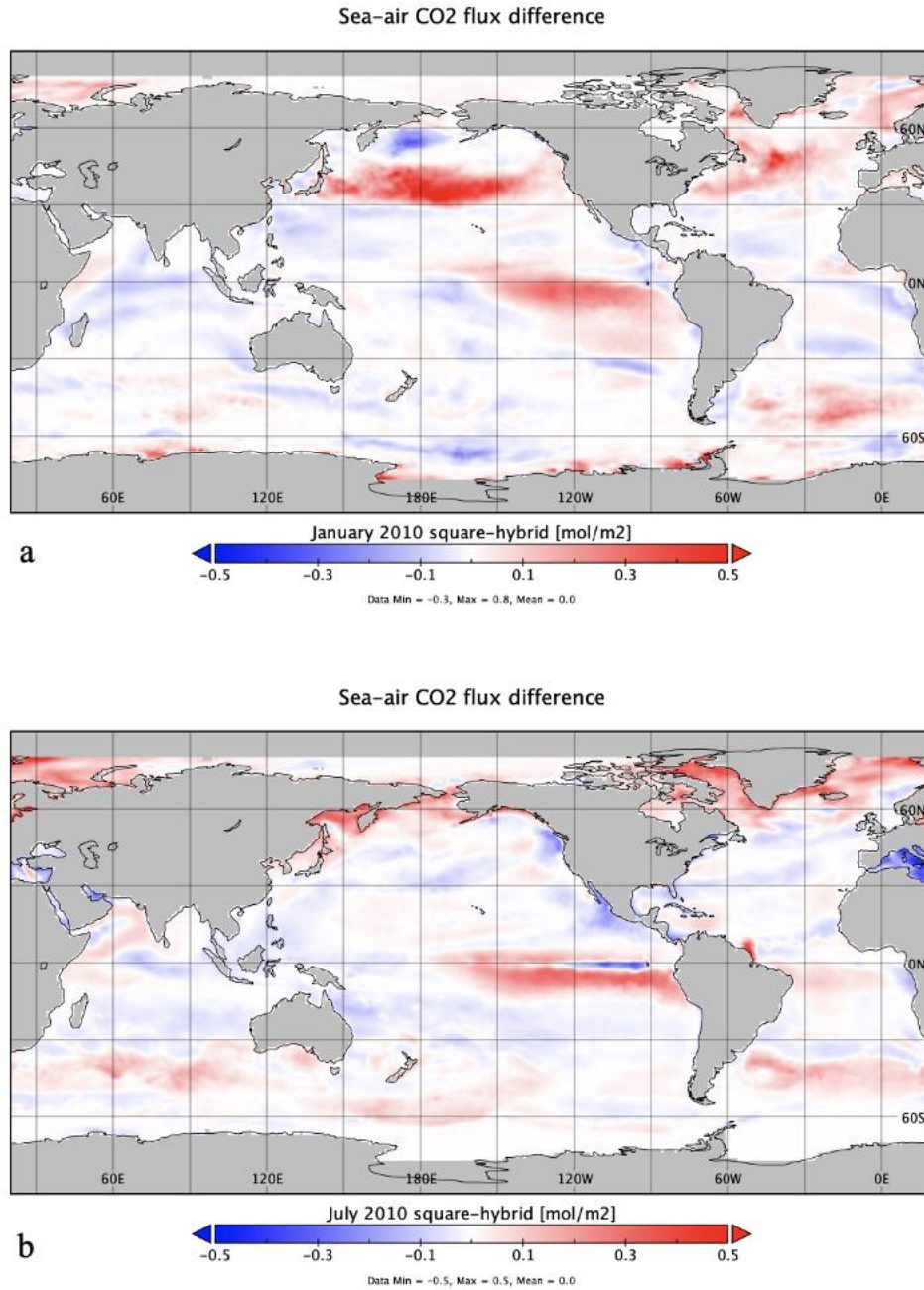
1071
10721073
1074
1075
1076
1077
1078
1079
1080
1081
1082

Figure 11. Monthly averaged air-sea CO₂ fluxes in the 30°-35°N latitude band using different XCO_{2a} products and the AOML_ET for fCO_{2w} values. The MBL XCO_{2a} product (solid line; solid circles) and PBL XCO_{2a} product (dashed lines; open circles) are shown versus month for 2010. The blue lines are zonally averaged fluxes for 30°-35°N; the green lines are fluxes over the Yellow Sea (30°-35°N); the red lines are the fluxes over the Mid-Atlantic Bight (30°-35°N). The horizontal solid and dashed blue lines are the annual average fluxes using the MBL and PBL products, respectively in the 30°-35°N latitude band.



1083
1084
1085
1086
1087
1088
1089
1090

Figure 12. Maps of differences in air-sea CO₂ fluxes between the square wind speed and hybrid relationships for gas transfer for January (a) and July (b) 2010 using AOML_ET. The flux densities for January and July using AOML_ET and the default wind speed squared relationship are shown in Figure 4. Color bar has units of [mol m⁻² y⁻¹].

1091 Table 1. Summary of magnitude variability and trends of global air-sea CO₂ fluxes from
 1092 different Machine Learning Approaches. Annual data from
 1093

1094	Study ^a	Average 1998- 2020 ^b	Trend ^c	r ^{2,d}	StError ^e	Flux 1998 ^f	Flux 2020 ^g
1097			Pg C decade ⁻¹			Pg C	Pg C
1098		Pg C				Pg C	Pg C
1099	AOML_ET	-1.70	-0.89	0.92	0.19	-0.72	-2.54
1100	<i>AOML_ET_AOnly</i>	<i>-1.60</i>	<i>-0.97</i>	<i>0.88</i>	<i>0.25</i>	<i>-0.49</i>	<i>-2.42</i>
1101	<i>AOML_ET-Chla</i>	<i>-1.82</i>	<i>-0.87</i>	<i>0.86</i>	<i>0.24</i>	<i>-0.71</i>	<i>-2.33</i>
1102	<i>AOML_ET_MLD</i>	<i>-1.72</i>	<i>-0.87</i>	<i>0.88</i>	<i>0.23</i>	<i>-0.80</i>	<i>-2.28</i>
1103	<i>AOML_ET+<U²></i>	<i>-1.72</i>	<i>-0.94</i>	<i>0.93</i>	<i>0.17</i>	<i>-0.71</i>	<i>-2.72</i>
1104	<i>AOML_ET_ΔfCO₂</i>	<i>-3.60</i>	<i>-0.55</i>	<i>0.91</i>	<i>0.12</i>	<i>-3.22</i>	<i>-3.99</i>
1105							
1106	MPI-SOMFFN	-1.91	-0.79	0.93	0.15	-1.17	-2.56
1107	Jena-MLS	-1.99	-0.51	0.63	0.26	-1.83	-2.60
1108	CMEMS	-1.94	-0.63	0.92	0.13	-1.54	-2.88
1109	GRaCER	-2.12	-0.57	0.95	0.09	-1.74	-2.66
1110	JMA-MLR	-2.36	-0.50	0.77	0.19	-2.18	-3.25
1111	NIES_NN	-2.01	-0.98	0.93	0.18	-1.24	-3.42
1112	CSIR	-2.08	-0.79	0.96	0.11	-1.53	-3.02
1113	UoEx	-2.43	-0.83	0.92	0.17	-1.90	-2.89
1114	Average ^h	-2.06	-0.7	0.88	0.16	-1.53	-2.87
1115	Min. ^h	-1.70	-0.5	0.63	0.09	-0.70	-2.54
1116	Max. ^h	-2.43	-0.98	0.96	0.26	-2.18	-3.42
1117							
1118							
1119							
1120							

- 1121 a. All data, except AOML-ET are from <https://globalcarbonbudget.org/carbonbudget/>. AOML
 1122 ET: AOML Extra Trees (this work); MPI-SOMFFN (Landschützer et al., 2016); Jena-MLS
 1123 (Rödenbeck et al., 2022); CMEMS (Chau et al., 2022): GRaCER (Gregor & Gruber, 2021);
 1124 NIES_NN (Zeng et al., 2014); JMA-MLR (Lida et al., 2021); CSIR(Gregor et al., 2019)
 1125 UoEx (Watson et al., 2020)
- 1126 b. Twenty-three year average (1998-2020) of the annual global values for each approach in Pg
 1127 C
- 1128 c. Trend based on a linear regression of the twenty three years of annual global air-sea CO₂
 1129 fluxes in Pg C decade⁻¹
- 1130 d. Coefficient of determination
- 1131 e. Standard error from the linear trend
- 1132 f. Global air-sea CO₂ flux in 1998 for each of the methods
- 1133 g. Global air-sea CO₂ flux in 2020 for each of the methods
- 1134 h. Average, minimum, and maximum of the methods (listed in bold) excluding the
 1135 permutations of AOML_ET (in italics).
 1136
 1137